International Journal of Plasticity 203 (2026) 104744

Contents lists available at ScienceDirect

International Journal of Plasticity

journal homepage: www.elsevier.com/locate/ijplas

Characterization of dislocation networks under varying boundary conditions in the discrete to continuum transition regime

Balduin Katzer [a,b,*], Daniel Weygand [a], Katrin Schulz [a,b,*]

[a] Karlsruhe Institute of Technology (KIT), Institute for Applied Materials (IAM), Kaiserstr. 12, 76131 Karlsruhe, Germany
[b] Karlsruhe University of Applied Sciences (HKA), Moltkestr. 30, 76133, Karlsruhe, Germany

ARTICLE INFO

Keywords:
Boundary condition
Crystal plasticity
Dislocation dynamics
Dislocation network
Pre-straining

ABSTRACT

The formation and evolution of dislocation networks governs the plastic response and the mechanical properties of crystalline materials, influencing yield strength, strain hardening and ductility. However, identifying representative dislocation network features that can be transferred to continuum formulations such as crystal plasticity is challenging due to the complexity of the evolving dislocation structures.

In this study, we employ three-dimensional discrete dislocation dynamics (DDD) simulations of face-centered cubic (fcc) single crystalline metals to explore how dislocation networks affect plasticity under homogeneous (tension, shear) and gradient-induced (bending, torsion) boundary conditions. Our analysis reveals three fundamental dislocation network characteristics: (i) the dislocation link length distribution, (ii) the degree of link pinning, and (iii) the proximity of links to free surfaces. From the physics of bow-out and lengthening we derive an exponential envelope probability that captures the long tail of the link length distribution and is independent of the imposed boundary condition. We report pinning mechanisms due to successive dislocation interactions between links on different slip systems impeding subsequent link motion. By analyzing pre-strained inhomogeneous dislocation networks generated by a strain path change, we reveal that these pinning mechanisms selectively enhance or suppress dislocation multiplication demonstrating how prior deformation reshapes subsequent plasticity.

Ultimately, we embed the derived dislocation network descriptors in a probabilistic dislocation-based plasticity model. The proposed model predicts dislocation multiplication, plastic shear and strain hardening for various crystal orientations, reproduces size effects and demonstrates the importance of dislocation network characteristics for continuum modeling.

1. Introduction

The emergence of dislocation networks during plastic deformation of crystalline materials due to the motion and the subsequent mutual interaction of dislocations has been known and studied for more than half a century (Amelinckx, 1956; Arsenlis and Parks, 1999; Carrington et al., 1960; Franciosi et al., 1980; Hirsch et al., 1956, 1958; Hirth, 1961; Taylor, 1934). However, identifying representative dislocation network characteristics for continuum modeling and crystal plasticity is still challenging due to the arising complexity of dislocation networks influenced by both the initial microstructure and boundary conditions. As in-situ experimental observations of dislocation networks are still limited to extremely small volumes and loading conditions within the experimental setup, several studies investigated dislocation interaction mechanisms and their contribution to strain hardening as well as to

* Corresponding authors.
E-mail addresses: balduin.katzer@kit.edu (B. Katzer), katrin.schulz@kit.edu (K. Schulz).

https://doi.org/10.1016/j.ijplas.2026.104744
Received 14 March 2026; Received in revised form 12 May 2026
Available online 5 June 2026

dislocation multiplication for continuum modeling employing in-silico methods such as molecular dynamics (MD) (Bulatov et al., 2006; Zepeda-Ruiz et al., 2020) or discrete dislocation dynamics (DDD) simulations (Csikor et al., 2007; Devincre et al., 2008; El-Awady, 2015). And while several observations regarding the dislocation density evolution have been successfully implemented into continuum modeling (Castelluccio and McDowell, 2017; Roters et al., 2019; Sudmanns et al., 2019; Schulz et al., 2019; Vivekanandan et al., 2021), the physical link between dislocation network evolution and continuum description is still incomplete for several reasons.

First, DDD simulations have shown that dislocation multiplication is dominated by the weakest link mechanism, which represents only a fraction of the entire dislocation density (El-Awady et al., 2009; Senger et al., 2011b; Berta et al., 2025b). Recently, it was shown that the length of dislocations within dislocation networks follow an exponential distribution (Voyiadjis and Yaghoobi, 2017; Sills et al., 2018; Katzer et al., 2023; Akhondzadeh et al., 2026) implying that few long dislocations, which represent the weakest links, contribute the most to plasticity. With the rise of statistically informed crystal plasticity models, the capability of incorporating discrete slip events in continuum modeling has been shown (Wijnen et al., 2021; Jeong and Voyiadjis, 2022; Ye et al., 2023a,b; Ruestes and Segurado, 2024; Wijnen et al., 2025; Lamari et al., 2025). Especially, the implementation of link length distributions (Ye et al., 2023a,b) leading to stress distributions due to the Orowan mechanism enabled the incorporation of dislocation network information in crystal plasticity. However, as most studies investigated homogeneous loading conditions, the analysis of gradient-imposed loading conditions is of importance due to the emergence of inhomogeneous dislocation microstructure evolutions in bending (Higashida et al., 1986; Motz et al., 2008; Chen et al., 2010), torsion (Weinberger and Cai, 2010; Senger et al., 2011a; Gravell et al., 2021; Stricker et al., 2022) or indentation (Gagel et al., 2016; Song et al., 2019). Thus, the origin and the universality of dislocation link length distributions as well as their incorporation into continuum modeling is still not answered satisfactorily especially when considering varying boundary conditions.

Second, MD and DDD simulations revealed the origin of naturally pinning of dislocations within face-centered cubic (fcc) single crystalline materials (Motz et al., 2009; Wang et al., 2024) due to the occurrence of subsequent dislocation-dislocation reactions, also known as dislocation jamming (Ispánovity et al., 2014; McDowell, 2025). These pinning points exhibit stable anchors to dislocations and are generated by the intersection point of at least three interacting glide planes leading to zero degree freedom. These pinning points can lead to opposing effects such as increased dislocation multiplication due to a spiral source mechanism for dislocations pinned on one side (Motz et al., 2009; Weinberger and Cai, 2011; Cui et al., 2014) as well as to hardening due to anchored dislocation pinned on both sides (Motz et al., 2009; Wang et al., 2024). Thus, quantifying the effect of pinning on plasticity in dislocation networks has to be addressed.

Third, DDD simulations revealed that inhomogeneous initial dislocation networks can lead to significantly different dislocation microstructure evolution (Kohnert and Capolungo, 2022). These inhomogeneous initial dislocation networks can arise e.g. from pre-straining of samples, which is often conducted experimentally to increase the initial dislocation density from annealed samples (Bei et al., 2008; Lee et al., 2009; El-Awady et al., 2013; Schneider et al., 2013; Song et al., 2019; Li et al., 2023). Studies on pre-straining, which focused primarily on the investigation of size effects, revealed opposing results on the mechanical response, i.e. leading to either increasing (Schneider et al., 2013) or decreasing (Lee et al., 2009; El-Awady et al., 2013) flow stresses, or no-effect at all (Schneider et al., 2013). Thus, the effect of pre-straining on plasticity leading to inhomogeneous dislocation networks has to be further addressed with respect to dislocation multiplication and plastic shear.

In this study, we investigate dislocation network characteristics employing three-dimensional DDD simulations applying homogeneous (tension, shearing) and gradient-imposed (bending, torsion) boundary conditions for varying crystal orientations to answer the aforementioned aspects, We explore whether dislocation link length distributions are affected by the natural occurrence of pinning or by the applied boundary conditions due to heterogeneous local stresses and slip system dependent Schmid factors. Based on our analyses, we derive an exponential envelope probability for the link length distribution based on dislocation bow-out and lengthening naturally yielding to the occurrence of long dislocation link lengths. In addition, we study the effect of inhomogeneous dislocation networks generated by pre-straining leading to enhanced and suppressed dislocation multiplication and plasticity originating from pre-generated dislocation junctions, shifted link length distributions as well as heterogeneous slip system dependent dislocation density distributions. Furthermore, we develop a probabilistic dislocation-based plasticity model incorporating the derived dislocation network characteristics. We demonstrate the applicability of the proposed plasticity model for varying crystal orientations as well as for different specimen sizes naturally leading to size effect related mechanisms such as different flow stresses or stress drops.

2. Methods

2.1. Discrete dislocation dynamics simulation

In this work, we employ three-dimensional discrete dislocation dynamics (DDD) simulations to study evolving dislocation network characteristics during plasticity of single crystalline metals. Detailed information about the 3D DDD code and the boundary value problem implementation is provided in Weygand et al. (2001, 2002). Specimens represent fcc Aluminum micropillars with an aspect ratio of 1:2:1 and with a thickness t of 3 µm, a length of 6 µm and a width of 3 µm (if not stated otherwise). The material properties of Aluminum are chosen with the shear modulus $\mu = 27\,\mathrm{GPa}$, the Poisson's ratio $\nu = 0.347$, the lattice constant $a = 0.4045\,\mathrm{nm}$ and the drag coefficient $1\times10^{-4}\,\mathrm{Pa\,s}$ for both screw and edge dislocations. Cross-slip is enabled in the DDD simulations using a probability term (Verdier et al., 1998; Weygand et al., 2002), which is described in more detail in Appendix I. We study two types of dislocation network configuration, namely *pristine* and *pre-strained* dislocation networks (see Fig. 1(a)). Pristine dislocation

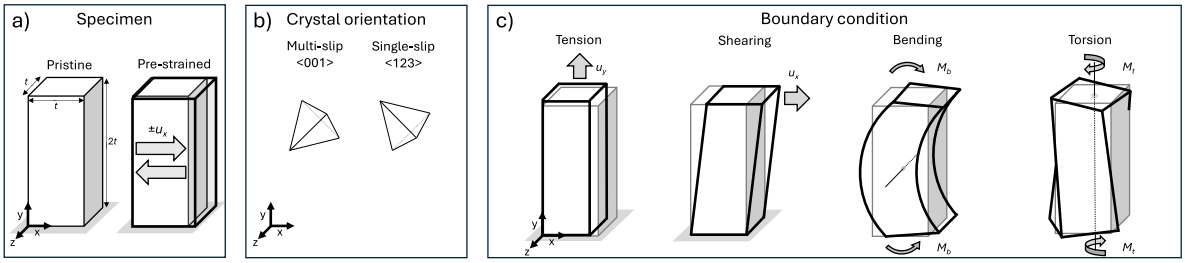

Fig. 1. Overview of the 3D DDD simulation setup. (a) The considered specimens contain initially either relaxed or pre-strained dislocation networks. (b) The effect of crystal orientation is studied for ⟨001⟩ multi-slip and ⟨123⟩ single-slip. (c) Homogeneous (tension, shearing) and gradient-imposed (bending, torsion) boundary conditions are applied.

networks, are relaxed artificial pinning point free configurations described in Appendix A. Pre-strained dislocation networks are generated from the pristine dislocation network with a subsequent loading routine employing a tensile test with subsequent relaxation along the thickness direction as described in Appendix B. In addition, we consider two crystal orientations, the ⟨001⟩ multi-slip as well as ⟨123⟩ single-slip orientation (see Fig. 1(b)). Thus, for the ⟨001⟩ sample, we pre-strain along the ⟨100⟩ crystal orientation and for the ⟨123⟩ sample, we pre-strain along the $\langle 11\bar{1}\rangle$ crystal orientation. For statistics, we investigate five initial dislocation networks for each pristine and pre-strained sample each in both crystal orientations. These networks represent the starting point for the subsequent loading scenarios.

2.2. Boundary conditions

In this study, we analyze the dislocation microstructure evolution under four different boundary conditions, namely tension, simple shearing, pure bending and pure torsion loading as shown as a sketch in Fig. 1(c). The finite element method (FEM) is employed to solve the elasto-static equilibrium equations for each boundary conditions and compute the stress tensor fields that drive dislocation motion. Detailed information about the implementation is provided in Weygand et al. (2001, 2002, 2008). We apply the four displacement-controlled boundary conditions as follows:

- Tension: We apply a constant strain rate $\dot{\varepsilon} = 2000\,\mathrm{s}^{-1}$ along y-direction at the top surface $\mathrm{y}_{\max}$ leading to a displacement u_y while the bottom surface at $\mathrm{y}_{\min}$ is fixed in y-direction. All other surfaces are traction free and rigid body motion and rotation are suppressed (Weygand and Gumbsch, 2005; Stricker and Weygand, 2015; Katzer et al., 2022). For the analysis of the mechanical response, we evaluate the stress $\sigma_{\mathrm{ten}} = \sigma_{\mathrm{yy}}$ and the total strain $\varepsilon_{\mathrm{yy}}$ in tensile direction.
- Shearing: We apply a constant strain rate $\dot{\varepsilon} = 2000\,\mathrm{s}^{-1}$ along x-direction by imposing u_x displacements at the $\mathrm{y}_{\max}$ surface while the bottom surface at $\mathrm{y}_{\min}$ is fixed. All other surfaces are traction free. For the analysis of the mechanical response, we evaluate the total shear stress $\sigma_{\mathrm{she}} = \tau_{\mathrm{xy}}$ and the total shear strain $\varepsilon_{\mathrm{xy}}$.
- Bending: To obtain a constant bending moment M_B (pure bending) and thus a nearly homogeneous deformation state along the beam axis, displacement boundary conditions $u_\mathrm{y}(x)$ are prescribed with respect to x and the beam thickness t in order to deduce the tensile and compressive stresses in the beam leading to a average σ_{yy} of zero as detailed in Motz et al. (2008). All remaining surfaces are traction free. We apply a constant strain rate $\dot{\varepsilon} = 2000\,\mathrm{s}^{-1}$ along x-direction at $0.5\,\mathrm{y}_{\max}$. For the analysis of the mechanical response, the normalized bending moment $\sigma_{\mathrm{ben}} = M_\mathrm{B}/(b\,t^2)$ with the width $b = t$ and the normalized displacement $u^{\mathrm{y,max}}/t$ is determined.
- Torsion: To impose a torsion moment M_T, a constant torsion angle rate $\dot{\varphi} = 1.4°\,\mathrm{s}^{-1}$ is prescribed: the top surface $\mathrm{y}_{\max}$ rotates clockwise, whereas the bottom surface $\mathrm{y}_{\min}$ rotates counter clockwise. The rotation is realized by prescribing corresponding displacements $u_\mathrm{x}(\varphi)$ and $u_\mathrm{z}(\varphi)$ at the top resp. bottom surfaces (Senger et al., 2011a). The y-direction at top/bottom and all other surfaces are traction free. This corresponds to a surface shear strain rate of $\dot{\gamma} \approx 3000\,\mathrm{s}^{-1}$ on the mid point position of the sides. For the analysis of the mechanical response, we report the normalized torsion moment $\sigma_{\mathrm{tor}} = M_\mathrm{T}/t^3 = 2.24\,\mu\,\varphi/4$ and the torsion angle φ (Senger et al., 2011a).

2.3. Dislocation network features

In this study, we utilize metrics to quantify dislocation microstructure characteristics employing a graph database (Katzer et al., 2024a). To quantify the dislocation density ρ, we decompose ρ into N dislocation links. Each link of length L carries the information of its slip system ξ (slip plane normal $\mathbf{n}$, Burgers vector $\mathbf{b}$). In addition, each link is described by the geometrical pinning condition of its end-nodes leading to unpinned, semi-pinned or double-pinned links (Motz et al., 2009). Unpinned dislocation links have no constraints in motion other than the glide plane. The end nodes of dislocation links can be geometrically pinned due to dislocation interactions leading to semi-pinned dislocation links anchored at one end only and double-pinned dislocation links pinned at both ends. Since, we study the effect of loading conditions, we describe each dislocation link by its location in terms of in-volume, which

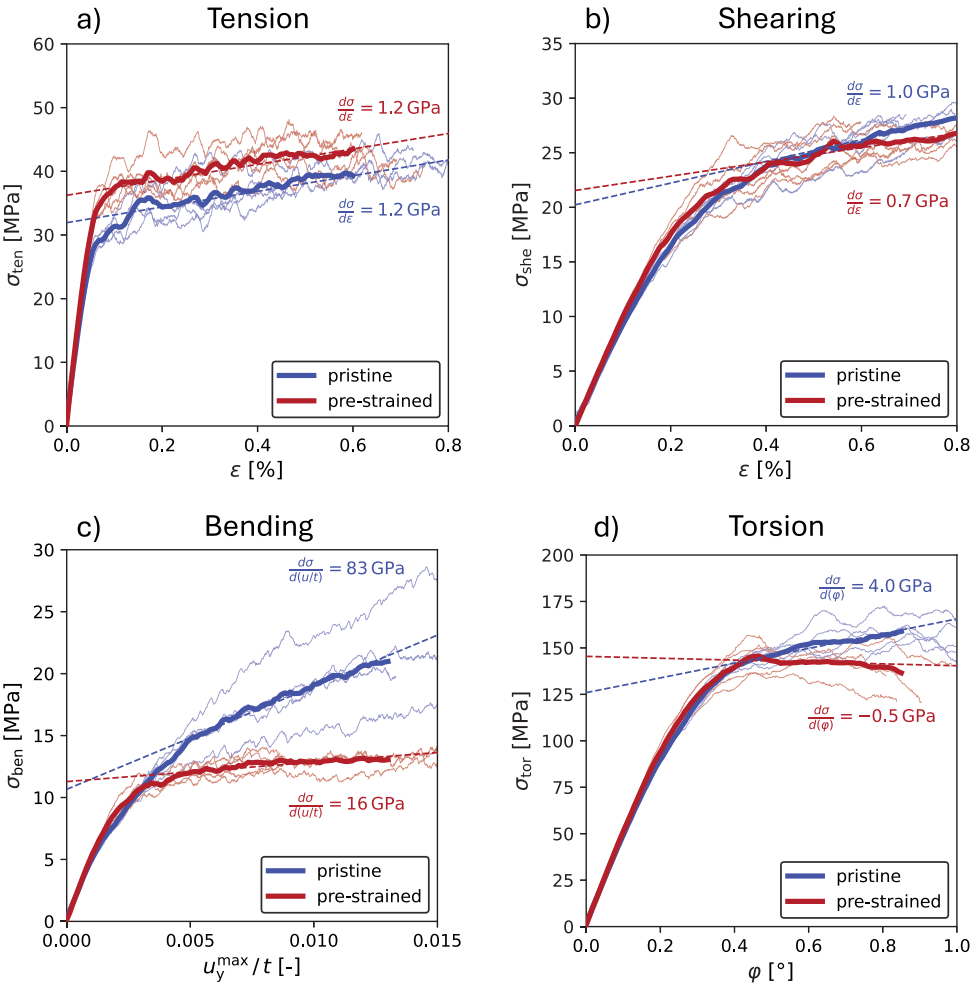

Fig. 2. The mechanical response due the applied boundary conditions in ⟨001⟩ crystal orientation for (a) tension, (b) shearing, (c) bending and (d) torsion. Thick lines depict the mean and thin lines the individual mechanical response for pristine and pre-strained dislocation networks.

resembles bulk-like behavior, or near-surface position. A dislocation link is considered as near-surface if the distance of the center of the link is closer than $t/10$ to any surface, which is approximately $1/\sqrt{\rho}$, otherwise it is considered as in-volume. To characterize the dislocation link length probability, the exponential probability density distribution (Sills et al., 2018) is employed using

$$P(L/\bar{L}) = \frac{1}{\bar{L}} \exp(-(L/\bar{L})), \tag{1}$$

where $\bar{L} = 1/\sqrt{\rho}$ is the average link length.

3. Results

3.1. Mechanical response due to the applied boundary conditions

The mechanical response and dislocation network characteristics of different initial samples are examined for four loading cases: two homogeneous conditions (tension and shear) and two gradient-imposed conditions (bending and torsion). Fig. 2 illustrates the mechanical response of the specimens with a ⟨001⟩ crystal orientation subjected to (a) tension, (b) shearing, (c) bending, and (d) torsion. The mechanical response shows a distinct behavior for the pristine and the pre-strained dislocation network. For tension (a), the flow stress of the pre-strained sample is larger than for the pristine sample, whereas the hardening rate is similar with 1.2 GPa. For shearing (b), the flow stress is similar and the hardening rate is lower for the pre-strained samples compared to the pristine samples. Bending (c) reveals a significantly larger hardening rate for pristine specimens than pre-strained specimens. In addition, the mechanical response shows larger scatter for pristine specimens. For torsion (d), same flow stresses behavior at initial

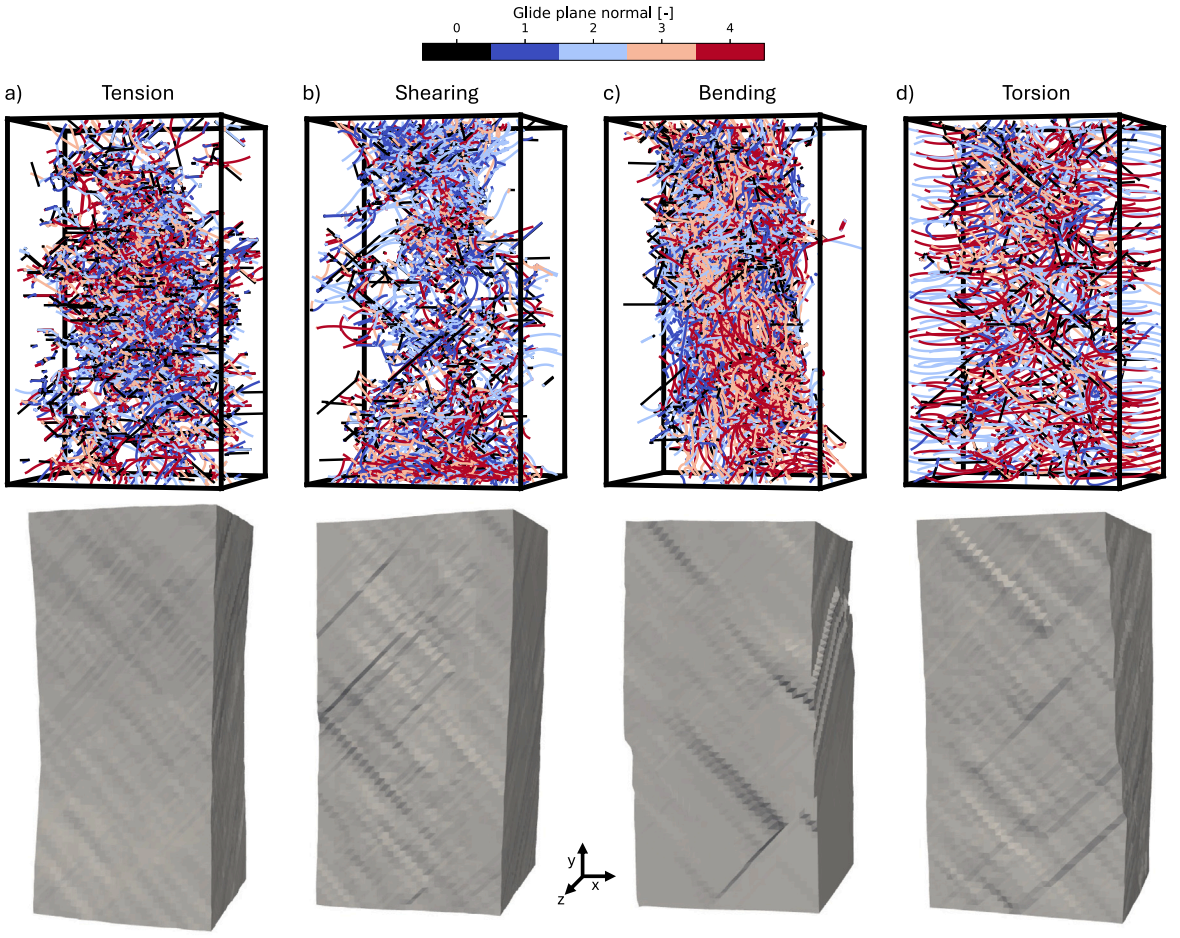

Fig. 3. Three-dimensional visualization of exemplarily chosen representative dislocation networks color-coded by the glide plane normal where 0 represents physical dislocation junctions (top row) and the deformed micropillars due to the applied boundary conditions in ⟨001⟩ crystal orientation for (a) tension, (b) shearing, (c) bending and (d) torsion (bottom row).

yielding of pristine and pre-strained specimens are observed. The hardening rate differs with higher hardening for pristine than for pre-strained specimens. Overall, the differences between pristine and pre-strained specimens are visible for the onset of yielding in tension as well as for the hardening rate in shearing, bending and torsion. The evolution of the total dislocation densities for each loading scenario are shown in Appendix D and reveal similar total dislocation multiplication rates for pristine and pre-strained specimens.

The four loading scenarios result in distinct dislocation networks as illustrated in Fig. 3. Under tension (a), dislocations preferentially accumulate within the central region of the specimen leading to a pronounced densification of the network. In contrast, shearing (b) drives dislocations towards the top and bottom surfaces, where the highest resolved shear stresses occur, as well as towards the center of the specimen. Bending (c) produces dislocation density along the neutral plane of the y-axis reflecting high tensile and compressive forces near the x_{min} and x_{max} surfaces. Torsion (d) generates curved dislocation structures concentrated near the outer radius arising from the increasing stress with radial distance from the central y-axis at x_{mid} and z_{mid}.

Similar to the ⟨001⟩ crystal orientation, the mechanical response of specimens oriented along ⟨123⟩ crystal orientation is shown in Fig. S1. Overall, hardening is less pronounced than in the ⟨001⟩ orientation. The flow stress under shear loading is higher for pre-strained samples compared to pristine samples. The three-dimensional visualizations in Fig. S2 highlight the formation of dislocation networks governed by the activation of slip systems distinct from those in the ⟨001⟩ orientation. For shearing and bending, a similar pattern of dislocation network densification is observed. In contrast, tension produces only limited densification in the core while torsion leads to dislocation accumulation along the y-axis in specific spatial regions.

3.2. Dislocation link statistics

This section illustrates the characteristics of dislocation link lengths and their dependence on the four loading conditions for the ⟨001⟩ crystal orientation at the maximal deformation studied here. Fig. 4(a) shows the probability distribution $P(L/\bar{L})$

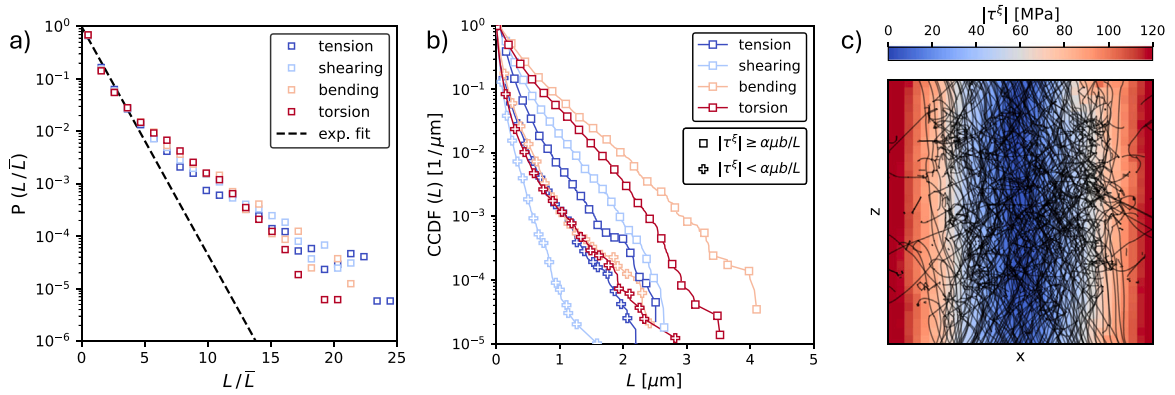

Fig. 4. The link length probability with respect to applied stress in ⟨001⟩ crystal orientation for all loading scenarios. (a) The link length probability follows a exponential distribution (Eq. (1)) for link lengths below $3\,L/\bar{L}$ and shows an increased probability for larger link lengths independent of the applied boundary condition. (b) CDDF of dislocation link lengths L shows large links where the resolved shear stress exceeds the Taylor yield stress with $\alpha = 0.4$. (c) Example of dislocation link arrangement, which included pile-ups, on one specific slip system ξ due to bending around z-axis leading to shear stress τ^{ξ}.

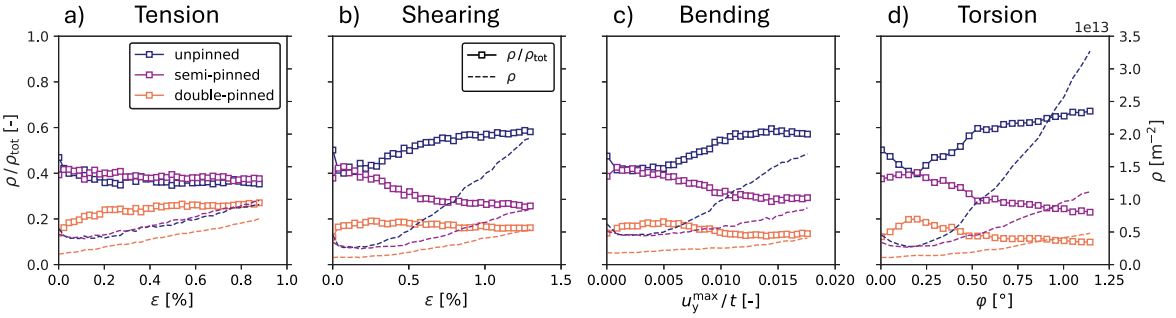

Fig. 5. The dislocation density ρ and the fraction ρ/ρ_{tot} of unpinned, semi-pinned and double-pinned dislocation links for (a) tension, (b) shearing, (c) bending and (d) torsion in ⟨001⟩ crystal orientation.

of the normalized link length $L/\bar{L}$. For all loading conditions, normalized link lengths below $\approx 3\,L/\bar{L}$ follow the exponential distribution (Eq. (1)) as indicated by the dashed line. Beyond this link length ($L/\bar{L} \geq 3$), the probability distribution deviates from the exponential distribution, revealing an increased occurrence of longer links regardless of the boundary condition. Fig. 4(b) shows the complementary cumulative distribution function (CCDF) of link length with respect to the effective resolved shear stress $\tau_{\text{eff}} = |\tau| - \alpha\mu b/L$, where τ is the applied shear stress on the considered slip system ξ of the dislocation link, μ the shear modulus, b the Burgers vector modulus, and α a constant accounting for Taylor hardening and line tension effects chosen to be 0.4. The CCDF reveals the fraction of dislocation links, which exceed a certain link length. For $\tau_{\text{eff}} < 0$, dislocation links are shorter compared to regions, where the local yield stress exceed the yield stress ($\tau_{\text{eff}} \geq 0$). For bending and torsion, longer link lengths are observed compared to tension and shearing for $\tau_{\text{eff}} \geq 0$. Fig. 4(c) illustrates an example of a dislocation link arrangement ans shear stress τ^{ξ} for a particular slip system ξ under bending around z-axis viewed in a cross section of the sample. The dislocation structure under bending shows as main feature dislocation pile-ups and densification towards the center. The pile-up structure reduces dislocation junction formation and thus leads to longer links visible in the CCDF.

During glide motion and dislocation reactions, dislocation links can be geometrically pinned. Fig. 5 shows the evolution of the dislocation density ρ and the fraction ρ/ρ_{tot} of unpinned, semi-pinned and double-pinned dislocation links for the four applied loading scenarios and ⟨001⟩ crystal orientation. For tension, the fraction of unpinned and semi-pinned dislocation links reaches to $\approx 37\%$ and the fraction of double-pinned dislocation links increases to $\approx 25\%$. For the other loading scenarios, the fraction of double-pinned dislocation links either remains at $\approx 15\%$, or even decreases to $\approx 10\%$ for torsion loading. However, the fraction of unpinned and semi-pinned dislocation links changes during the onset of plasticity and reaches to $\approx 60\%$ (and to $\approx 65\%$ for torsion) of unpinned and to $\approx 25\%$ of semi-pinned dislocation links for the maximal deformation studied here.

Fig. 6 shows the dislocation link length probability distribution for the different pinning states (unpinned, semi-pinned, double-pinned). Across all loading conditions, links that are double-pinned follow the exponential distribution (Eq. (1)) closely with only a few more elongated links for tension, shearing and bending for normalized link lengths of $L/\bar{L} \geq 7$. This suggests that pinning

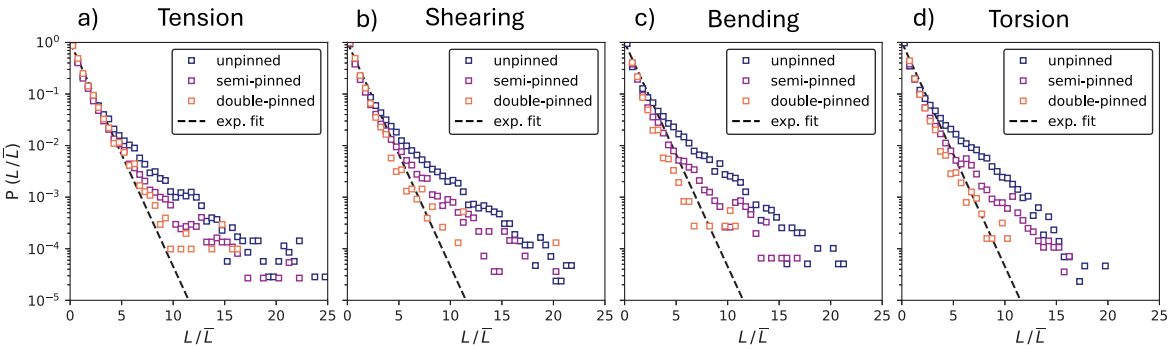

Fig. 6. The link length probability with respect to pinning arising from dislocation interactions for (a) tension, (b) shearing, (c) bending and (d) torsion in ⟨001⟩ crystal orientation. Double-pinned link lengths follow a exponential distribution (Eq. (1)), whereas semi-pinned exhibit an increased and unpinned an even more increased probability for long link lengths.

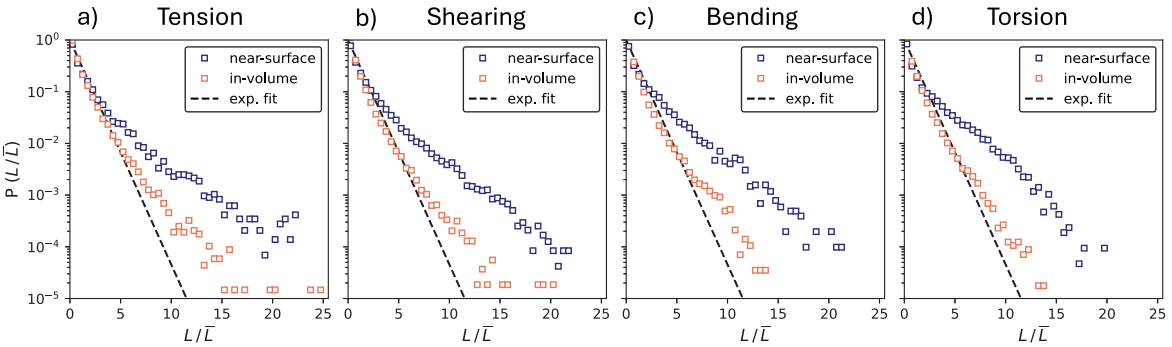

Fig. 7. The link length probability with respect to the spatial position for (a) tension, (b) shearing, (c) bending and (d) torsion in ⟨001⟩ crystal orientation. In-volume link lengths follow the exponential distribution more closely compared to near-surface links.

reduces significantly the probability for link elongation under applied stress. In contrast, semi-pinned links exhibit a noticeable deviation from the exponential trend for larger normalized link lengths ($L/\bar{L} \geq 6$), indicating an increased probability of forming extended links. The most pronounced deviation occurs for unpinned links, which show an even higher probability for the occurrence of long link lengths compared to semi-pinned configurations transition at $L/\bar{L} \geq 3$. This trend is observed consistently across all loading conditions, implying that the absence of pinning constraints enables unrestricted link growth under stress-driven conditions. However, all link length distributions up to $L/\bar{L} = 3$ follow the exponential distribution (Eq. (1).

Fig. 7 shows the link length probability distribution for two spatial categories namely near-surface and in-volume (which resembles bulk-like behavior). Across all loading conditions, links exhibit a distribution that closely follows an exponential distribution for link lengths $L/\bar{L} < 3$. For dislocation links with $L/\bar{L} \geq 3$, in-volume links tend to follow the exponential distribution more closely than near-surface links. The shape of the probability distribution of the near-surface link lengths slightly differs among the studied loading conditions.

To confirm the importance of the resolved shear stress, Fig. 8 shows the link length distribution broken down to slip systems for tensile loading. The distributions are normalized by their respective $\bar{L}^{\xi}$. Under tension, the externally applied stress is uniform within the specimen, enabling a clear interpretation of slip system activity. On inactive slip systems $\xi = 3, 4, 9, 10$ (A3, B4, C3, D4), see Table 1, the dislocation links lengths follows the exponential distribution. The remaining eight active slip system with Schmid factor of $S^{\xi} = 0.41$ reveal similar dislocation link length distributions $P(L/\bar{L}^{\xi})$. This observations holds true for pristine as well as for pre-strained samples, where $\bar{\rho}^{\xi}$ is $\approx 50\%$ larger on active slip systems indicating that lengthening is more dependent on the current applied stresses and less dependent on previous deformation.

For specimens with a ⟨123⟩ crystal orientation similar observations for the link length statistics are made. Lengthening of dislocation links takes place only for links, where the resolved shear stress overcomes the local yield stress as shown in Fig. S3. The fraction of unpinned and semi-pinned dislocation links diverges slightly larger and a lower amount of double-pinned dislocation links is present for shearing, bending and torsion. Pinning and spatial position of dislocation links reveal the same behavior as for the ⟨001⟩ crystal orientation as shown in Fig. S5 and in Fig. S6, respectively. The slip system dependent analysis in Fig. S7 reveals large deviations from the exponential distributions for slip systems with Schmid factors $S^{\xi} \geq 0.2$.

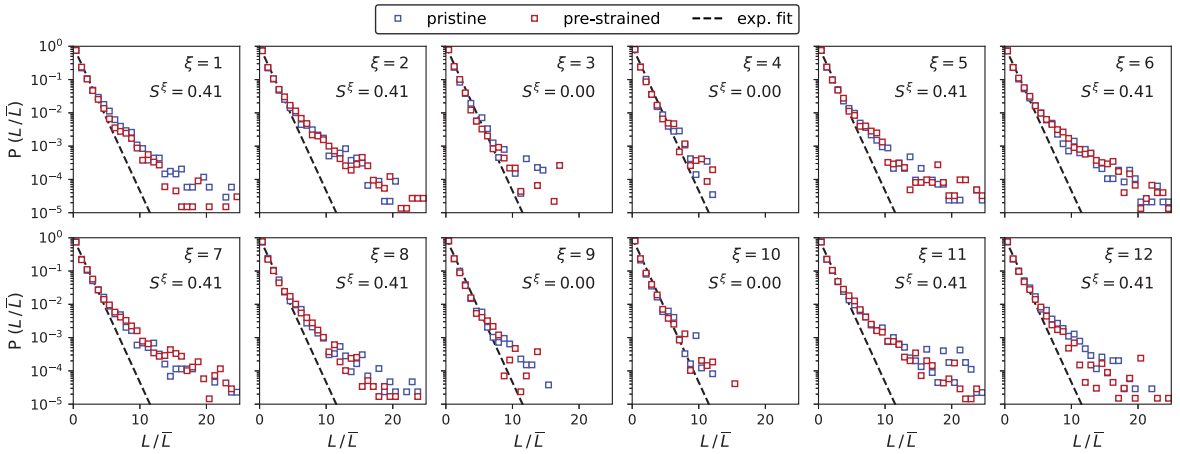

Fig. 8. The link length probability with respect the slip system ξ for pristine and pre-strained samples and normalized by their respective $\bar{L}^\xi$ marked as $\bar{L}$.

Table 1
Schmid factors S^ξ per slip system ξ for fcc slip systems for ⟨001⟩ crystal orientations loading conditions as well as for the pre-straining along the ⟨100⟩ crystal orientation (cp. Appendix C).

Schmid-Boas	A6	A2	A3	B4	B5	B2	C1	C5	C3	D4	D1	D6
Slip system ξ	1	2	3	4	5	6	7	8	9	10	11	12
Pre-strained ⟨100⟩	0.41	0.00	0.41	−0.41	−0.41	0.00	0.00	0.41	−0.41	0.41	0.00	−0.41
Tension	−0.41	−0.41	0.00	0.00	0.41	0.41	−0.41	−0.41	0.00	0.00	0.41	0.41
Shearing	0.00	0.41	−0.41	−0.41	0.00	0.41	−0.41	0.00	−0.41	−0.41	−0.41	0.00
Bending	0.41	0.41	0.00	0.00	0.41	0.41	0.41	0.41	0.00	0.00	0.41	0.41
Torsion	0.41	0.41	0.58	0.58	0.41	0.41	0.41	0.41	0.58	0.58	0.41	0.41

Slip plane normal **n**				Burgers vector **b**					
A	B	C	D	1	2	3	4	5	6
$(1\bar{1}\bar{1})$	(111)	$(\bar{1}11)$	$(\bar{1}\bar{1}\bar{1})$	[011]	$[01\bar{1}]$	[101]	$[\bar{1}01]$	$[\bar{1}10]$	[110]

3.3. Pinning of dislocations

Pinning of dislocation links occurs due to consecutive mutual dislocation-dislocation interactions. The origin of pinned end nodes of dislocation links are numerous. Since the employed DDD simulation tracks the swept area and generation of each dislocation junction (Weygand et al., 2002), we can follow the dislocation pinning mechanisms. To provide examples of pinning mechanisms, Fig. 9 shows three frequently observed dislocation link configurations. In (a), we observe a semi-pinned link including a glissile reaction at the unpinned node leading to links on system A6, A3 and B2. The pinned node at the bottom, the first reaction has been a glissile reaction including system A6 and D1 leading to a link on system D4. Subsequently, D1 interacted with B5 dissolving D1 and leading to a Lomer junction and subsequently a pinned node. In (b), we observe a semi-pinned link with a coplanar reaction involving links on system A2, A6 and A3 at the unpinned node. The pinned node at the bottom interacts several times including a combination of a glissile, a Lomer and a collinear reaction. First, a glissile reaction is generated by A2, C3 leading to A6, followed by a collinear reaction transforming A6 to D6 and finally followed by a Lomer reaction generated by D6 and C3 leading ultimately to the pinned end node with a link on A2 and a Lomer junction only similar to a spiral source (Motz et al., 2009). In (c), we observe a double-pinned dislocation link. At the bottom node, we observe a combination of a Lomer and a cross-slip reaction. First a Lomer junction is generated by A6 and C1, followed by cross-slip of C1 to D1, ultimately leaving a pinned end node. At the top node, we observe a combination of a glissile and a collinear reaction. First a glissile reaction leads to a A6, B2 and A3 triplet, followed by an additionally collinear reaction transforming A3 to C3, ultimately leaving a pinned node. Ultimately, these examples should demonstrate the variety of different pinning mechanisms of dislocation links based on a combination of dislocation multiplication (glissile, coplanar, cross-slip) and dislocation stabilization (collinear, Lomer, Hirth) reactions.

3.4. Impact of pre-straining on dislocation network evolution

Pre-straining affects the mechanical response of the considered micropillars as shown in 3.1. This deviation must originate from the initial dislocation network structure and its evolution. Fig. 10 illustrates the structural changes of initial dislocation networks induced by pre-straining based on the Burgers indices, where 0 represents physical dislocation junctions. The Burgers index is used

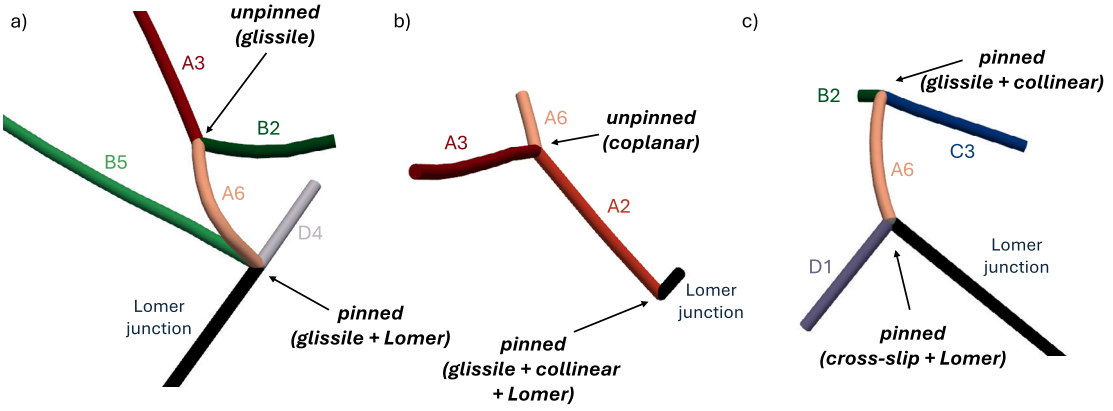

Fig. 9. Three dislocation link configurations with different pinning status. (a) A semi-pinned link with a pinned node due to glissile and Lomer reactions. (b) A semi-pinned link with a pinned node due to glissile, collinear and Lomer reactions. (c) A double-pinned link with a first pinned node due to glissile and collinear reactions and a second pinned node due to cross-slip and Lomer reactions.

here for color coding, since the Schmid factors S^{ξ} for pre-straining along $\langle 100 \rangle$ can be subdivided into two inactive Burgers indices 1,2 and four active Burgers indices $3, 4, 5, 6$ as shown in Table 1. The top row exemplarily compares the initial pristine network (left) with the initial pre-strained network (right) in three dimensions and through a two-dimensional projection of a sub-volume along the y-axis. The visible densification of the dislocation network due to pre-straining leads to an increased number of short dislocation links. Fig. 10(a) shows that the link length distribution of the pristine dislocation network follows a exponential distribution (Eq. (1)). Due to the pre-straining routine along the x-axis (see Appendix B), dislocation links are activated on four Burgers indices (eight slip systems) leading to an increase in dislocation density as shown in Fig. 10(b), where the error bars indicate the standard deviation from five simulations each. This increase reflects the selective activation of slip systems under the applied load and is consistent with the Schmid factors consideration. In addition, an increase of long dislocation links with activated Burgers indices is present after pre-straining as shown in Fig. 10(c). This indicates that pre-straining not only increases dislocation density but also promotes the elongation of dislocation links, which persist even after subsequent unloading and relaxation. The presence of long links suggests that pre-straining introduces stable dislocation link configurations.

To identify the initial differences of stable configurations, Fig. 11 shows network characteristics with respect to pinning and junction formation. As shown in Fig. 11(a), the dislocation density distribution among all slip systems ξ has changed due to pre-straining based on the activation of eight slip systems in $\langle 100 \rangle$ crystal orientation (cp. Fig. 10 as well as Table 1). In addition, the dislocation density of physical dislocation junctions (Lomer, Hirth) indicated by slip system $\xi = 0$ is significantly increased for pre-strained samples. The majority of junctions is double-pinned or at least semi-pinned. To understand the impact of dislocation junctions on the slip system dependent plasticity, we analyze, to which dislocation links the dislocation junctions are attached.[1] Fig. 11(b) shows that Lomer junctions are equally distributed for pristine samples for all slip systems, whereas for pre-strained samples the fraction of Lomer junctions is decreased for the inactive slip systems (A2, B2, C1, D1) along the pre-strain direction in $\langle 100 \rangle$ crystal orientation. The fraction of glissile junctions is not affected by pre-straining, whereas the fraction of collinear junctions is significantly lower on the inactive slip systems as well. In addition, we observe that the increase of the double-pinned fractions due to pre-straining appears on all slip systems for Lomer, glissile and collinear reactions.

Fig. 12 illustrates the evolution of (a) dislocation density ρ^{ξ} and (b) plastic shear γ^{ξ} per slip system ξ for tension in $\langle 001 \rangle$ crystal orientation comparing pristine and pre-strained dislocation networks. For the pristine dislocation network, the dislocation density increases similarly across the eight active and four inactive slip systems, respectively, following the Schmid factors shown in Table 1). This observation holds true for the evolution of γ^{ξ}. In contrast, the pre-strained dislocation networks display a markedly different behavior for the dislocation multiplication and plastic shear. Here, the eight active slip systems with equal Schmid factor of $S^{\xi} = 0.41$ subdivide into two groups. The first group with slip systems A2, B2, C1, D1 shows enhanced multiplication while the second group with slip systems A6, B5, C6, D6 exhibit suppressed multiplication. In addition, the first group has a lower initial dislocation density due to pre-straining compared to the second group. The evolution of plastic shear subdivides into two groups as well, however, the onset of the deviation alters at a slightly later strain state. For bending, a similar deviation into distinct groups due to pre-straining is observed as shown in Fig. F.2. For shearing and torsion, such a deviation is not observed as shown in Fig. F.1 and Fig. F.3, respectively.

Specimens loaded in $\langle 123 \rangle$ crystal orientation reveal that pre-straining does not significantly alter dislocation multiplication and plastic shear for tension and bending as shown in Fig. S8 and in Fig. S10, respectively. For tension as well as for bending, the slip

[1] As an example, please refer to Fig. 9(c), where dislocation links on slip system D1 and A6 are attached to a Lomer junction and therefore both links are hindered in motion.

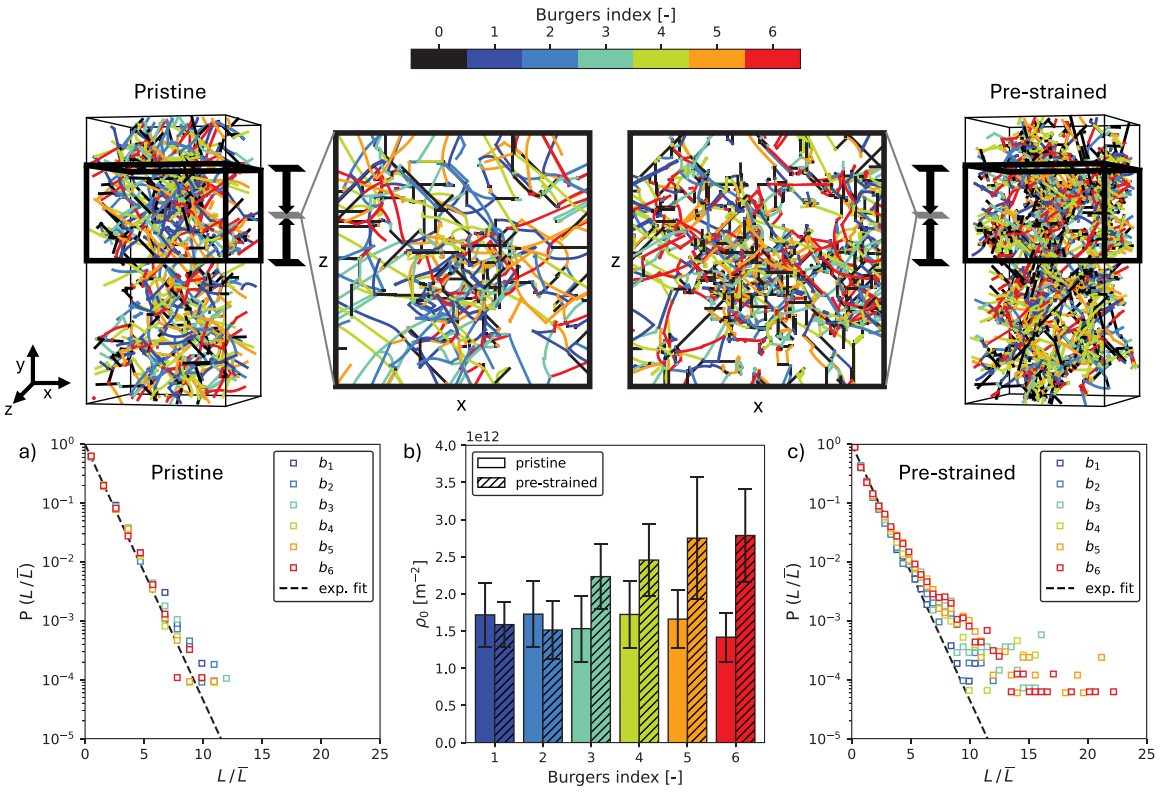

Fig. 10. The effect of pre-straining on the dislocation link characteristics in ⟨001⟩ crystal orientation. The top row shows exemplarily a pristine (left) and a pre-strained (right) dislocation network in 3D and of a 2D projection of a subvolume along the y-axis (color-coded by the Burgers index where 0 represents physical dislocation junctions). The link length distribution of the pristine dislocation network follows the exponential distribution (a). Due to pre-straining, specific Burgers indices are activated leading to an increase of dislocation density (b) and to elongation of these activated dislocation links in pre-strained dislocation networks (c) even after subsequent unloading an relaxation (see Appendix B).

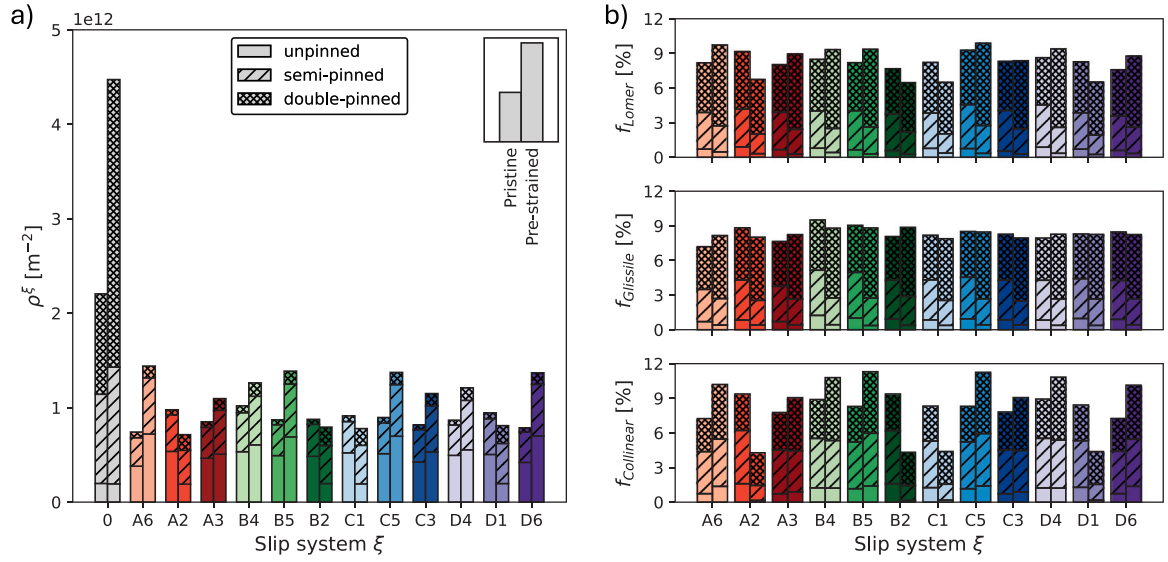

Fig. 11. (a) Initial dislocation density per slip system with respect to pinning for the pristine and pre-strained sample. (b) Fractions of Lomer, glissile and collinear junctions connected to dislocation links on slip system ξ.

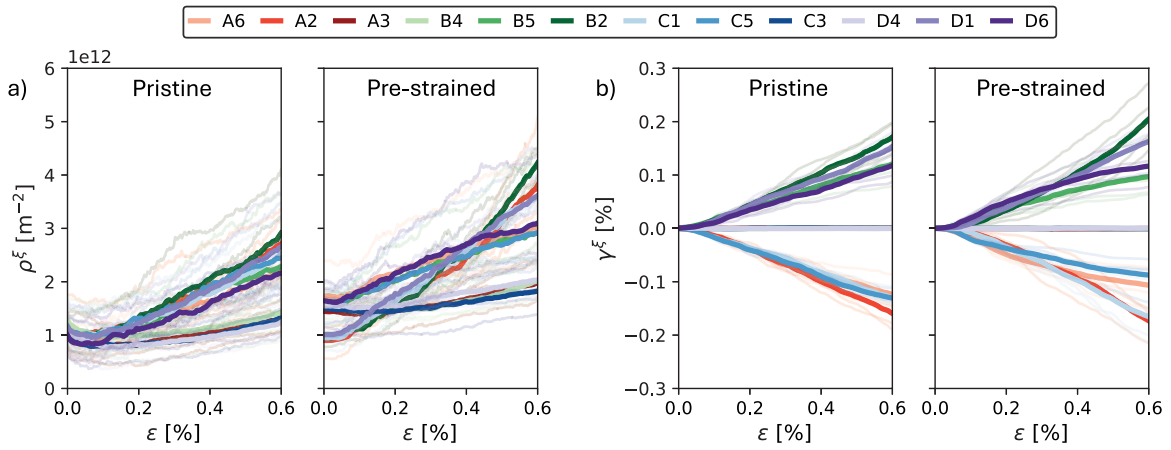

Fig. 12. The effect of pre-straining for tension in ⟨001⟩ crystal orientation on the evolution of (a) dislocation density ρ^{ξ} and (b) plastic shear γ^{ξ} per slip system ξ. The pre-strained dislocation networks leads to a suppressed and enhanced dislocation density evolution and plastic shear compared to pristine specimens. Bold lines indicate the mean behavior across the studies samples.

system A3 dominates the dislocation multiplication and the plastic slip for pristine and pre-strained samples. For bending, there is additional dislocation multiplication on the slip system C3 due to cross-slip. In contrast, shearing and torsion in ⟨123⟩ crystal orientation shows dislocation multiplication and plastic shear on additional slip systems due to pre-straining as shown in Fig. S9 and in Fig. S11, respectively. For shearing, pre-straining enables additional slip systems A6, A3, B4, B2 to contribute to dislocation multiplication and plastic shear in contrast to pristine samples, where only the slip systems C1 and C3 are activated. For torsion, the slip systems B5 and C5 additionally contribute to dislocation multiplication due pre-straining, whereas only C1 and D1 are active in pristine samples. However, in ⟨123⟩ crystal orientation the effect of enhanced and suppressed dislocation multiplication is less distinct and divisible into groups, and is more related to a larger number of activated slip systems in general.

4. A probabilistic dislocation-based plasticity model

4.1. Model description

To incorporate the derived characteristics of dislocation networks, namely the dislocation link length distribution, the degree of link pinning, and the proximity of links to free surfaces, into a continuum framework, we propose a probabilistic dislocation-based plasticity model outlined in Fig. 13. The model accounts for dislocation multiplication due to dislocation link lengthening as well as dislocation starvation resulting from the escape of dislocation links from the sample volume. Furthermore, plastic shear is included based on dislocation glide for unpinned dislocation links and dislocation bow-out for semi-pinned and double-pinned links.

Based on the findings from the DDD analyses, the formulation accounts for key characteristics of the dislocation network: Long dislocation links dominate plastic deformation due to their lower critical activation stress, consistent with a weakest link mechanism (Ispánovity et al., 2013). In contrast, short links rarely operate as dislocation sources because their activation requires comparatively high shear stresses (Sills et al., 2020). Instead, they primarily stabilize the dislocation network and contribute to hardening by acting as forest obstacles to mobile dislocation links. The role of dislocation links further depends on their pinning state. Dislocation links can act as sources once the applied stress is sufficient to trigger bow-out of the link (Motz et al., 2009). Double-pinned dislocation links correspond to potential static Frank-Read sources, unpinned links to dynamic sources, and semi-pinned links may operate as spiral sources (Motz et al., 2009).

In a continuum theory, a dislocation source is characterized by its link length L_{src}, which determines its critical activation stress

$$\tau_{\mathrm{src},j} = \frac{\beta_j \mu b}{L_{\mathrm{src}}}, \quad j = 0, 1, 2 \tag{2}$$

where β_j is a factor for the type of source (Shishvan and der Giessen, 2010). We adopt $\beta_2 = 1$ for double-pinned links, $\beta_1 = 0.5$ for semi-pinned links (similar to a quarter circle compared to a half circle bow-out) and $\beta_0 = 0.1$ for unpinned links. For each link within the dislocation network, this relation yield the activation stress $\tau_{\mathrm{src},j}(L_{\mathrm{src}}, \beta_j)$. Upon loading, a link L_{src} with pinned state j on slip system ξ operates as source when its resolved shear stress τ^{ξ} satisfies $\tau^{\xi} \geq \tau_{\mathrm{src},j}(L_{\mathrm{src}}, \beta_j)$.

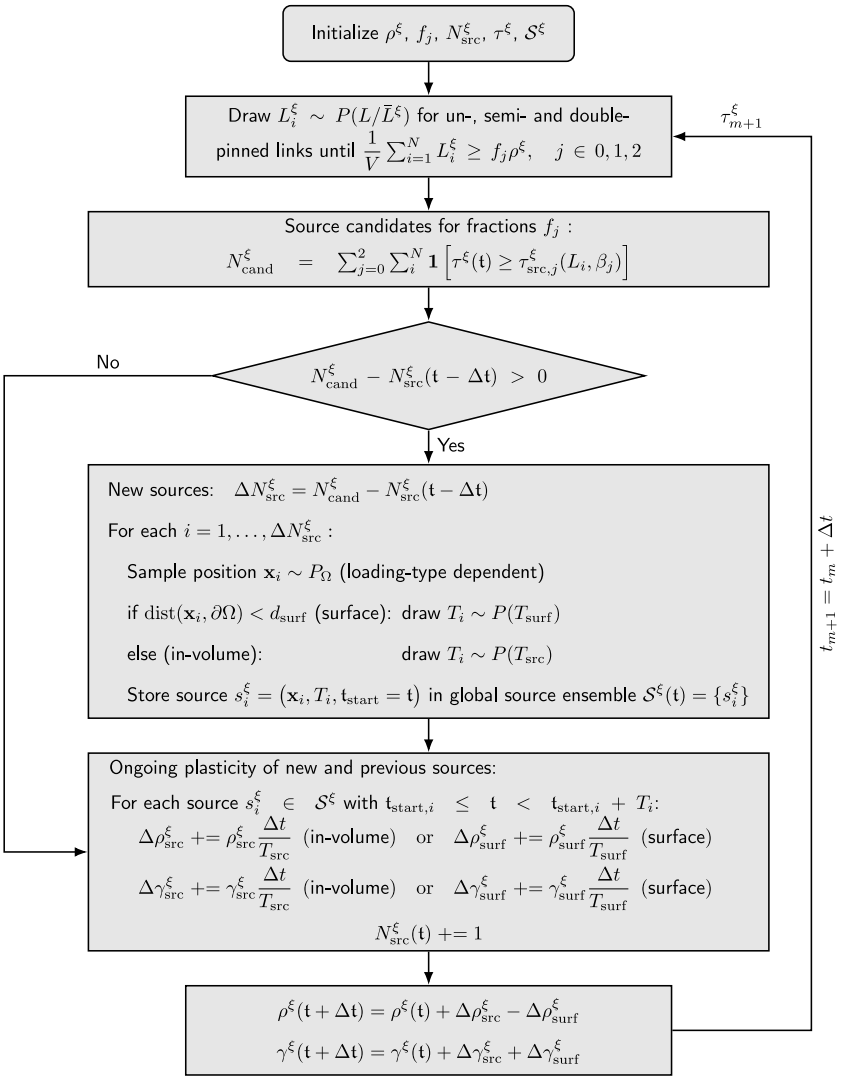

Fig. 13. Flow chart of the probabilistic dislocation-based plasticity model incorporating static (link length, pinning and surface proximity) and dynamic (dislocation reaction frequencies) dislocation network features.

To generate an ensemble of links for a given dislocation density ρ^ξ, links lengths are sampled from the probability density distribution $P(L/\bar{L}^\xi)$[2] until the dislocation density of the cumulative dislocation line length satisfies

$$\frac{1}{V}\sum_{i=1}^{N^\xi} L_i^\xi \geq \rho^\xi, \tag{3}$$

leading to N^ξ links on slip system ξ of lengths following $P(L/\bar{L}^\xi)$. The reference length scale $\bar{L}^\xi$ is defined from the mean dislocation density $1/\bar{\rho}^\xi$. Based on the fractions of unpinned (f_0), semi-pinned (f_1), and double-pinned (f_2) links obtained from the DDD simulations (cp. Fig. 5), we generate N_0^ξ, N_1^ξ, N_2^ξ links of each type, respectively. Subsequently, at each time step t, the shear stress τ^ξ is evaluated for each slip system ξ employing

$$\tau^\xi = \mathbf{M}^\xi \cdot \boldsymbol{\sigma} \qquad \mathbf{M}^\xi = \frac{1}{2}\left(\mathbf{d}^\xi \otimes \mathbf{n}^\xi + \mathbf{n}^\xi \otimes \mathbf{d}^\xi\right) \tag{4}$$

[2] For the explanation of the probabilistic plasticity model, we employ the exponential probability distribution $P(L/\bar{L}^\xi)$. However, for the presented results, it is replaced by the derived envelope probability distribution $P_{\mathrm{env}}(L/\bar{L}^\xi)$ from (Eq. (24)) derived in Section 5.1, where k_{min} starts with 1.0 at $\varepsilon = 0.0\%$ and linearly decreases to $k_{\mathrm{min}} = 0.4$ at $\varepsilon = 0.2\%$.

where $\mathbf{M}^{\xi}$ is the Schmid tensor defined by the normalized slip direction $\mathbf{d}^{\xi}$ of the Burgers vector $\mathbf{b}^{\xi}$ on the slip normal $\mathbf{n}^{\xi}$. Since each link of length L_i^{ξ} on slip systems ξ is associated with a critical source stress τ_{src} (cp. Eq. (2)), a link is considered as a source candidate if

$$\tau^{\xi} \geq \tau_{\mathrm{src},j}(L^{\xi}, \beta_j). \tag{5}$$

The total number of source candidates per slip system is then given by

$$N_{\mathrm{cand}}^{\xi} = \sum_{j=0}^{2} \sum_{i}^{N^{\xi}} \mathbf{1}\left[\tau^{\xi} \geq \tau_{\mathrm{src},j}(L_i^{\xi}, \beta_j)\right], \tag{6}$$

where $j = 0, 1, 2$ represents unpinned, semi-pinned and double-pinned sources, respectively. If the number of source candidates exceeds the number of already activated sources,

$$N_{\mathrm{cand}}^{\xi} - N_{\mathrm{src}}^{\xi}(\mathrm{t} - \Delta\mathrm{t}) > 0, \tag{7}$$

then $\Delta N_{\mathrm{src}}^{\xi} = N_{\mathrm{cand}}^{\xi} - N_{\mathrm{src}}^{\xi}(\mathrm{t} - \Delta\mathrm{t})$ additional sources are activated.

Next, a position $\mathbf{x}_i \sim P_{\Omega}$ is sampled for each source in $\Delta N_{\mathrm{src}}^{\xi}$, where P_{Ω} denotes a loading-condition dependent spatial distribution over the domain Ω. If the distance of $\mathbf{x}_i$ to any boundary is smaller than the distance d_{surf}, which is chosen to $1/\sqrt{\rho}$, the source is classified as near-surface and a characteristic surface emission period $T_i \sim P(T_{\mathrm{surf}})$ is sampled. Otherwise, the sources is treated as an in-volume source and samples with an activation period $T_i \sim P(T_{\mathrm{src}})$. The characteristic activation period is estimated from the reaction frequency $\nu_{\mathrm{src}} = 1/T_{\mathrm{src}}$, calculated as $\nu_{\mathrm{src}} = \Delta n_{reac}/(n_{links}\Delta\mathrm{t})$, where n_{reac} is the number of dislocation reactions tracked in the considered DDD simulations (Katzer et al., 2022). A Gaussian fit is employed to mimic the distribution as described in Appendix E. For simplicity, the surface emission distribution $P(T_{\mathrm{surf}})$ is assumed identical to $P(T_{\mathrm{src}})$.

Each source is then stored as $s_i^{\xi} = \left(\mathbf{x}_i, T_i, \mathrm{t}_{\mathrm{start}} = \mathrm{t}\right)$ in a global source ensemble $S^{\xi}(\mathrm{t}) = \{s_i^{\xi}\}$, where $\mathrm{t}_{\mathrm{start}}$ denotes the time of source generation. Plastic deformation is due to both the activation of newly generated sources and the continued activity of previously activated sources. Plasticity is generated by each source $s_i^{\xi} \in S^{\xi}$ during its respective time interval $\mathrm{t}_{\mathrm{start},i} \leq \mathrm{t} < \mathrm{t}_{\mathrm{start},i} + T_i$. Dislocation multiplication is expressed through the source density defined by the bow-out line length generated per unit volume V by all activated sources fulfilling Eq. (5),

$$\rho_{\mathrm{src}} = \frac{1}{V}\Delta L_{\mathrm{bow-out}}. \tag{8}$$

The bow-out is approximated as a semi-circle

$$\Delta L_{\mathrm{bow\text{-}out}}(L, d_{\mathrm{cut}}) = \begin{cases} \pi R & R \leq 2.5\bar{L}, \\ \pi R - 2R \arccos\left(\dfrac{d_{\mathrm{cut}}}{R}\right) & R > 2.5\bar{L}, \quad d_{\mathrm{cut}} = 2.5\bar{L}, \end{cases} \tag{9}$$

with using $R = L/2$. For long links ($L \geq \bar{L}$), the bow-out is truncated by a cutting distances d_{cut} with a maximum of $5\bar{L}$. Assuming simple kinetics, the corresponding increase in dislocation density over the time increment $\Delta\mathrm{t}$ is

$$\Delta\rho_{\mathrm{src}} = \rho_{\mathrm{src}} \frac{\Delta\mathrm{t}}{T_{\mathrm{src}}}. \tag{10}$$

Similarly, dislocation starvation occurs, when links classified as near-surface due to their spatial position, leave the specimen. The corresponding dislocation density contribution is $\rho_{\mathrm{surf}} = L_{\mathrm{surf}}/V$ leading to dislocation density annihilation using

$$\Delta\rho_{\mathrm{surf}} = \rho_{\mathrm{surf}} \frac{\Delta\mathrm{t}}{T_{\mathrm{surf}}}. \tag{11}$$

Plastic slip is determined by the swept area of dislocation links due to glide or bow out. For pinned links, bow-out is approximated by a semi-circle, with truncation applied for long links ($L \geq \bar{L}$). The swept area is

$$\Delta A_{\mathrm{bow-out}}(L, d_{\mathrm{cut}}) = \begin{cases} \frac{\pi}{2} R^2, & R \leq 2.5\bar{L}, \\ \frac{\pi}{2} R^2 - R^2 \arccos\left(\frac{d_{\mathrm{cut}}}{R}\right) + d_{\mathrm{cut}}\sqrt{R^2 - d_{\mathrm{cut}}^2}, & R > 2.5\bar{L}, \quad d_{\mathrm{cut}} = 2.5\bar{L}. \end{cases} \tag{12}$$

Unpinned and semi-pinned links contribute through motion with swept area

$$\Delta A_{\mathrm{motion}} = L\,\Lambda\,\frac{\Delta\mathrm{t}}{T_{\mathrm{src}}}, \tag{13}$$

where Λ denotes the mean free path, taken a $\min(\bar{L}, d_{\mathrm{surf}})$. The plastic shear increment on slip system ξ is therefore

$$\Delta\gamma_{\mathrm{src}} = \frac{b}{V}\left(\Delta A_{\mathrm{bow-out}} + \Delta A_{\mathrm{motion}}\right). \tag{14}$$

An analogous expression is used for dislocation sources near a surface $\Delta\gamma_{\text{surf}}$. Ultimately, each source s_i^ξ contributes to the evolution of dislocation density and plastic shear according to

$$\begin{aligned} \Delta\rho^\xi_{\text{src}} &\mathrel{+}= \rho^\xi_{\text{src}} \frac{\Delta t}{T_{\text{src}}}, \quad \Delta\rho^\xi_{\text{surf}} \mathrel{+}= \rho^\xi_{\text{surf}} \frac{\Delta t}{T_{\text{surf}}} \\ \Delta\gamma^\xi_{\text{src}} &\mathrel{+}= \gamma^\xi_{\text{src}} \frac{\Delta t}{T_{\text{src}}}, \quad \Delta\gamma^\xi_{\text{surf}} \mathrel{+}= \gamma^\xi_{\text{surf}} \frac{\Delta t}{T_{\text{surf}}} \\ N^\xi_{\text{src}}(\mathrm{t}) &\mathrel{+}= 1, \end{aligned} \tag{15}$$

resulting in a total number of $N^\xi_{\text{src}}(\mathrm{t})$ of active sources. The total dislocation density is updated at each time step using the current dislocation density $\rho^\xi(\mathrm{t})$, the generated source density $\Delta\rho^\xi_{\text{src}}$ and the annihilated near-surface density $\Delta\rho^\xi_{\text{surf}}$ as

$$\rho^\xi(\mathrm{t}+\Delta\mathrm{t}) = \rho^\xi(\mathrm{t}) + \Delta\rho^\xi_{\text{src}} - \Delta\rho^\xi_{\text{surf}} \tag{16}$$

and the plastic shear evolves according to

$$\gamma^\xi(\mathrm{t}+\Delta\mathrm{t}) = \gamma^\xi(\mathrm{t}) + \Delta\gamma^\xi_{\text{src}} + \Delta\gamma^\xi_{\text{surf}}. \tag{17}$$

The corresponding plastic strain tensor $\boldsymbol{\varepsilon}^{\text{pl}}$ is accumulated as

$$\Delta\boldsymbol{\varepsilon}^{\text{pl}}(\mathrm{t}+\Delta\mathrm{t}) = \sum_{\xi=1}^{12} \gamma^\xi(\mathrm{t}+\Delta\mathrm{t})\, \mathrm{M}^\xi. \tag{18}$$

This procedure is repeated for each time step t until the total time T is reached. The proposed plasticity model therefore captures dislocation multiplication and plastic slip per slip system while accounting for key dislocation networks characteristics, namely the link length distribution, pinning state and proximity to free surfaces.

4.2. Tensile loading

Exemplary, we apply the proposed probabilistic plasticity model to a tensile loading scenario in ⟨001⟩ crystal orientation as shown in Fig. 2(a) as well as in ⟨123⟩ crystal orientation as shown in Fig. S1(a) employing pristine samples. We use a finite element (FE) grid to generate the elastic stress field $\hat{\sigma}_{ij}(\mathrm{t})$ for $\mathrm{t} \in [0, T]$ for the boundary value problem. In this model, dislocation interactions are included only via the statistical measures, link length distribution and activation times, and thus no dislocation stress fields are included. Thus, for tensile loading along y-direction, the strain $\varepsilon_{yy}(\mathrm{t})$ is calculated from FEM. The plastic strain $\varepsilon^{\text{pl}}_{yy}(\mathrm{t})$ is accumulated from the slip activity yielding the mechanical response

$$\sigma_{yy}(\mathrm{t}) = E\, \varepsilon^{\text{el}}_{yy}(\mathrm{t}) = E\left(\varepsilon_{yy}(\mathrm{t}) - \varepsilon^{\text{pl}}_{yy}(\mathrm{t})\right). \tag{19}$$

The pinning fractions f_j are chosen in accordance to Fig. 5(a) and the characteristic activation time T_{src} and $T_{\text{surf}} = T_{\text{src}}$ are chosen in accordance to Fig. E.1. The spatial distribution of dislocation sources are assumed to be homogeneous for tensile loading employing $\mathbf{x}_i \sim \mathcal{U}(\Omega)$. The initial dislocation density $\rho^\xi(t_0)$ is chosen in accordance to a DDD simulation as shown in the initial state of Fig. 12(a).

Fig. 14 shows the models prediction of (a) the dislocation density ρ, (b) the plastic slip γ and (c) the stress–strain curve. The evolution of the dislocation density as well as the plastic deformation during plasticity closely follows the DDD simulation results. This leads to a resembling stress–strain response with a similar yield stress $\tau^{\text{y}}_{\text{p0.2\%}}$ and hardening. In addition, the model also captures stochastic plasticity features as avalanche like stress drops.

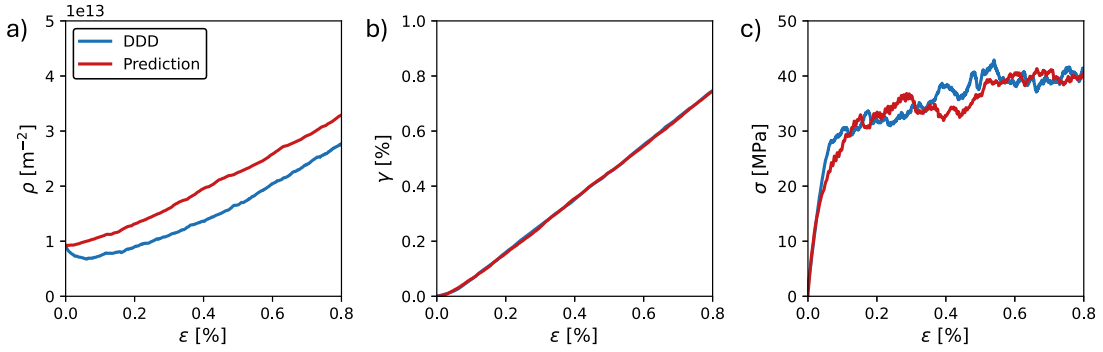

Fig. 14. Prediction of the plasticity model vs. the DDD simulation for tension in ⟨001⟩ crystal orientation including the dislocation density (a), plastic shear (b) and mechanical response (c).

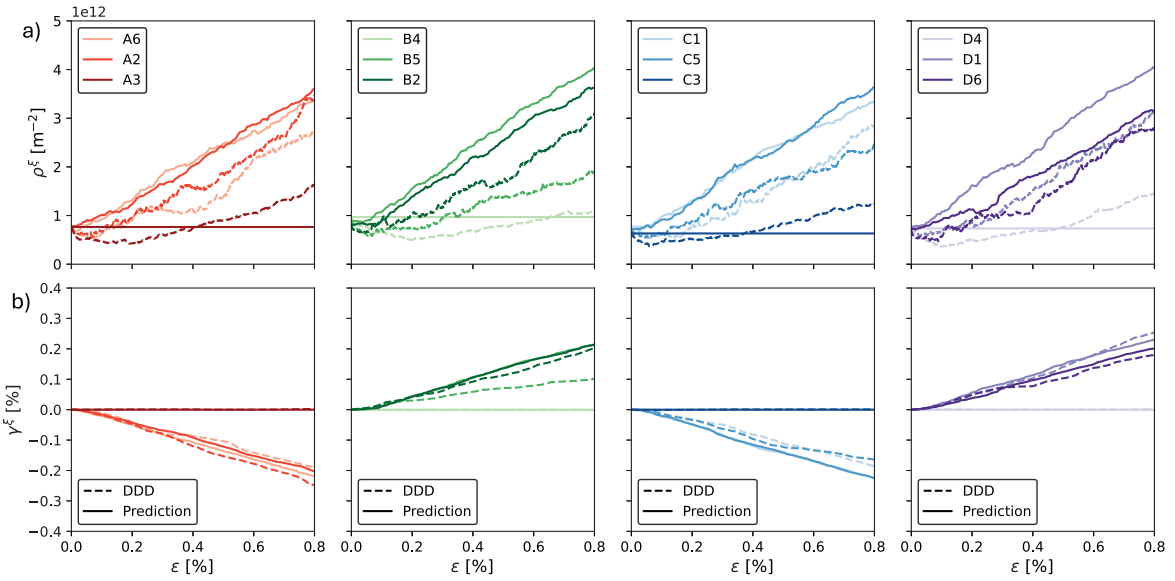

Fig. 15. Dislocation density evolution (a–d) and plastic shear (e–h) for tension in ⟨001⟩ crystal orientation.

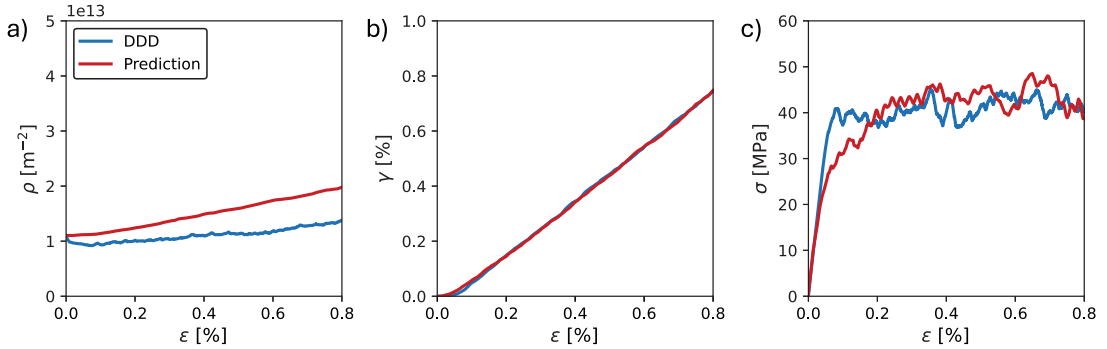

Fig. 16. Prediction of the plasticity model vs. the DDD simulation for tension in ⟨123⟩ crystal orientation including the dislocation density (a), plastic shear (b) and mechanical response (c).

Fig. 15 shows the evolution of (a) the dislocation density ρ^{ξ} and (b) the plastic slip γ^{ξ} per slip system ξ for the DDD simulation and the probabilistic plasticity model. The evolution of ρ^{ξ} and γ^{ξ} can be classified based on the Schmid factors S^{ξ} (cp. Table 1) into eight active and four inactive slip systems. The dislocation density evolution on active slip systems is slightly overestimated whereas the dislocation multiplication rate on inactive slip system is underestimated since no dislocation slip transfer is included. However, the overall trend is resembling between probabilistic plasticity model and DDD. The prediction of plastic shear per slip system is close to the DDD simulation as shown in Fig. 14(b). Active slip systems contribute equally to plasticity as they share the same Schmid factor, whereas inactive slip systems do not contribute to plastic shear.

Fig. 16 shows the probabilistic plasticity model prediction in ⟨123⟩ crystal orientation. Here, the pinning fractions f_0, f_1 and f_2 are chosen in accordance to Fig. S4. The initial dislocation densities per slip system are chosen in accordance to Fig. S8(a). The prediction of the dislocation density as well as the plastic shear resembles the DDD simulation, however, the dislocation density evolution is slightly overestimated. The stress–strain response is captured well by the probabilistic plasticity model including the low hardening rate for the ⟨123⟩ crystal orientation with a slightly higher yield stress $\tau^{y}_{\mathrm{p0.2\%}}$. Again, the probabilistic plasticity model captures avalanche like features during plastic deformation.

4.3. Size effects

To evaluate the transferability of the probabilistic dislocation-based plasticity model, we conducted DDD simulations for tension in ⟨001⟩ crystal orientation employing specimen sizes with thicknesses of 1 µm and 5 µm and an aspect ratio of 1:2:1 as shown in

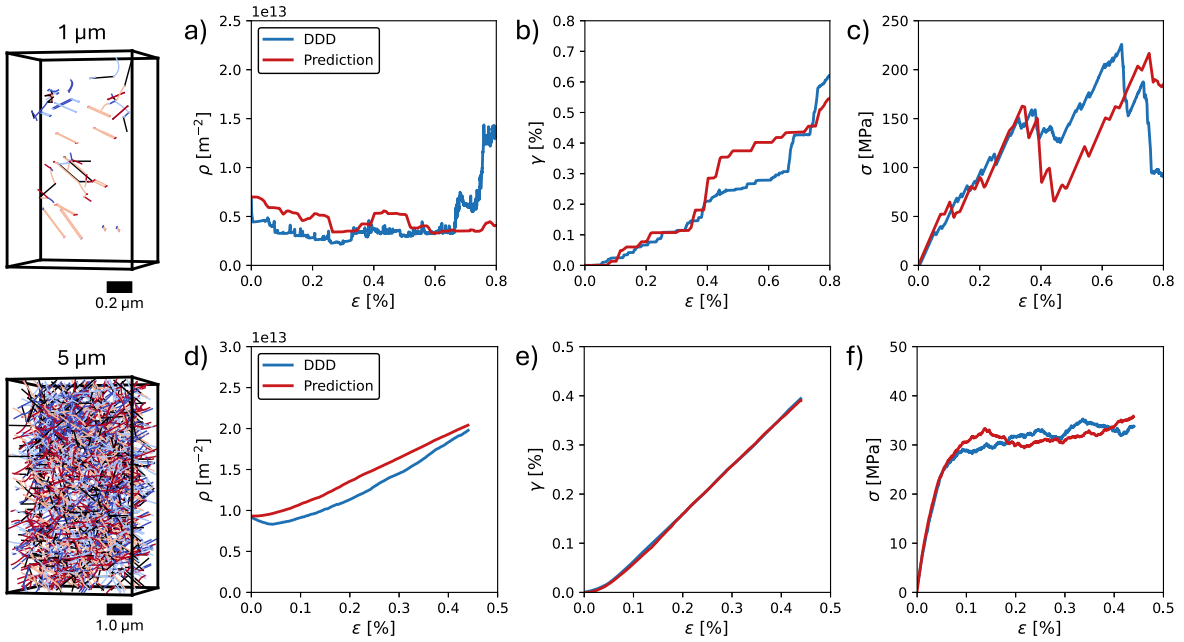

Fig. 17. Modeling size effects for tension in ⟨001⟩ crystal orientation for a 1 µm (top row) and a 5 µm (bottom row) sample employing the probabilistic plasticity model. Panels (a–c) and (d–f) show the evolution of dislocation density, plastic shear and stress–strain, respectively.

Fig. 17. The small sample has an initial dislocation density of around $0.5 \times 10^{12}\mathrm{m}^{-2}$ and the large of $1.0 \times 10^{12}\mathrm{m}^{-2}$, respectively. We employ the pinning fractions f_0, f_1 and f_2 from Fig. 5(a) and choose the activation period based on Gaussian fit of the reaction frequency distributions shown in E.1(c). The dislocation density evolution, the plastic shear as well as the mechanical response are shown in (a–c) for the small sample and in (d–f) for the large sample. For the small sample, the evolution of dislocation density is dominated by dislocation starvation due to near-surface links. The plastic shear changes rapidly (stair-case) similar to the DDD simulation results. The mechanical response reveals a similar stress–strain response including the size effect related high flow stresses larger than 100 MPa. For the large sample, the evolution of dislocation density is majorly dominated by dislocation multiplication due to in-volume links and the prediction follows the DDD simulation. Similarly, the prediction of plastic shear is close to the DDD simulation results. The mechanical response reveals that the flow stress is predicted well with a yield stress $\tau^{\mathrm{y}}_{\mathrm{p0.2\%}}$ of ≈ 30 MPa and similar hardening. The simulated and predicted yield stresses are in good agreement with experimental observations of Aluminum micropillar compression tests as shown in Appendix K.

4.4. Uncertainty quantification

To quantify how uncertainty propagates in the probabilistic dislocation-based plasticity model when applied to different specimen sizes, 50 independent model realizations are conducted. Fig. 18 summarizes the resulting uncertainty for the evolution of dislocation density, plastic shear and the resulting mechanical response for specimens with thicknesses of 1 µm and 3 µm. For the 1 µm specimen, the uncertainty of dislocation density (a) and plastic shear (b) evolution is comparatively large and increases with strain, reflecting the strong influence of the stochastic dislocation distribution and the dislocation starvation of near-surface links. The resulting mechanical response (c) exhibits a wide uncertainty range with increasing strains reflecting the strong sensitivity of the stress response to stochastic dislocation activation, multiplication and exhaustion. In contrast, the 3 µm specimen exhibits significantly narrower uncertainty bands as the higher number of statistically independent in-volume dislocation multiplication events leads to effective averaging and a more stable evolution of dislocation density, plastic shear and resulting mechanical response. This corresponds to a transition towards a bulk-like, statistically averaged response with reduced variability.

5. Discussion

5.1. Origin of link length distribution

In this study, we investigated dislocation network characteristics for homogeneous loading conditions (tension, shearing) as well as for gradient-imposed loading conditions (bending, torsion) for two different crystallographic orientations. First, the link length distribution exhibits a comparable probability density distribution independent of the loading condition (cp. Fig. 4(a)). This

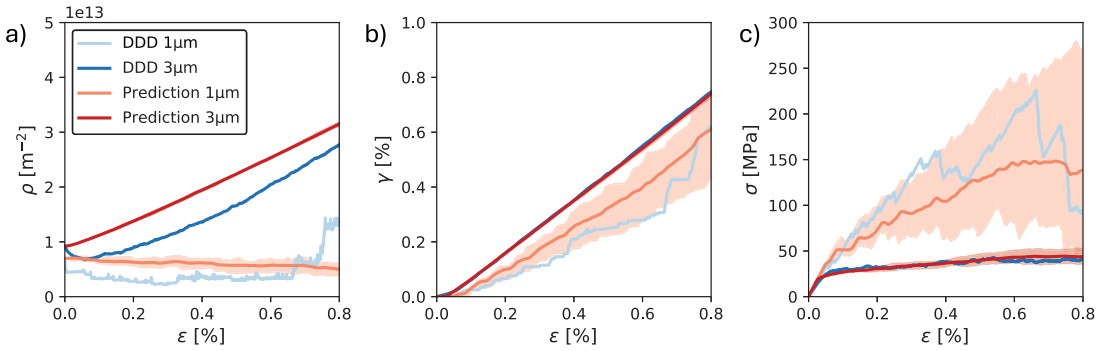

Fig. 18. Quantifying the uncertainty for tension in ⟨001⟩ crystal orientation for a 1 µm and a 3 µm sample employing the probabilistic plasticity model. Panels (a–c) show the evolution of dislocation density, plastic shear and stress, respectively, where the solid lines represent the mean response and the shaded regions denote the standard deviation.

observation is noteworthy because the dislocation networks visually differ markedly, as illustrated in Fig. 3. Second, the link lengths with $L/\bar{L} < 3$ follow an exponential distribution, consistent with previous reports (Sills et al., 2018; Katzer et al., 2023; Akhondzadeh et al., 2026). Third, for link lengths with $L/\bar{L} \geq 3$, the distribution deviates from the exponential form independent of the loading condition. The same deviation is observed for samples with a ⟨123⟩ crystal orientation as well (cp. Fig. S3(a)) and has also been reported for other crystal orientations (Akhondzadeh et al., 2026).

To capture the observed lengthening of dislocation links, we introduce two mechanisms (bow-out and lengthening by end-node motion) as shown in Fig. 19. Both mechanism are described by an exponential kernel $\Psi(L/\bar{L})$

$$\Psi(L/\bar{L}) = A\,\exp\left(-k\,(L/\bar{L})\right), \quad \text{with} \quad k = \bar{L}_0/\bar{L} \quad \text{and} \quad A = k^3 \tag{20}$$

adapted from the exponential distribution (Sills et al., 2018) with coefficient A and exponent k. $\bar{L}_0$ is the mean initial euclidean distance between the two end nodes of each dislocation link and $\bar{L}$ is the mean dislocation link length.

1. Bow-out mechanism (Fig. 19(a)): a straight link ($L = L_0$) yields $k = 1$ and recovers the exponential distribution Eq. (1). Bow-out to a semi-circular shape gives $L = \frac{\pi}{2}L_0$ and $k \approx 0.64$ and a full circular shape gives $L = \pi L_0$ and $k \approx 0.32$. Smaller k values increase the weight of long links, matching the tails observed in the DDD results (cp. Figs. 4, 6, 7).
2. End-node motion (Fig. 19(b)): the motion of the dislocation link end nodes extends a link from L_0 to L, e.g. lengthening of L_0 to $3L_0$ leads to $k \approx 0.33$. This mechanism also enriches the probability of long links.

The DDD simulations suggest that the actual link-length distribution results from a mixture of the two mechanisms, with the relative contribution depending on the pinning status and the proximity to free surfaces.

To describe the dislocation link length distribution due to both the bow-out and lengthening mechanisms, we introduce the envelope probability $P_{\text{env}}(L/\bar{L})$ using

$$P_{\text{env}}(x) = \frac{1}{C}\Psi_{\text{env}}(x), \qquad x = (L/\bar{L}) \tag{21}$$

with the normalization constant $C = 1 + 0.5e^{-3}\left(1 - k_{\text{min}}^2\right)$ and the non-normalized exponential envelop kernel

$$\Psi_{\text{env}}(x) = \sup_{k_{\text{min}} \leq k \leq 1} \Psi(x,k), \qquad x \geq 0, \quad k_{\text{min}} \geq 0, \tag{22}$$

defined as the supremum over the admissible range of the exponential kernel, where k_{min} is the smallest admissible value of the factor k. Using the exponential kernel $\Psi(x,k)$ and the optimizing function

$$k_{\text{opt}}(x) = \min\left(1, \max\left(k_{\text{min}}, \frac{3}{x}\right)\right) \tag{23}$$

the envelope probability (see Appendix G) can be written in closed form as

$$P_{\text{env}}(x) = \frac{\Psi_{\text{env}}(x)}{C} = \frac{1}{1 + \frac{e^{-3}}{2}(1 - k_{\text{min}}^2)}\left(k_{\text{opt}}(x, k_{\text{min}})\right)^3 \exp\left(-x\,k_{\text{opt}}(x, k_{\text{min}})\right), \qquad x = (L/\bar{L}), \quad x \geq 0. \tag{24}$$

Fig. 20(a) shows $\Psi_{\text{env}}(x)$ for several values of k_{min}. For $L/\bar{L} \leq 3$ the dislocation link lengths follow the exponential probability with $k = 1$ in agreement with Sills et al. (2018). For longer dislocation links the distribution follows the envelope probability down to the prescribed k_{min}. Fig. 20(b) demonstrates that a single envelope probability $\Psi_{\text{env}}(x)$ with a $k_{\text{min}} = 0.4$ fits the overall link-length data for all loading conditions for bulk-like behavior (cp. Appendix K). Furthermore, the envelope probability can be adapted to specific sub-populations (pinned, slip-system dependent, or near-surface links) shown in Section 3.2 by choosing an appropriate k_{min}.

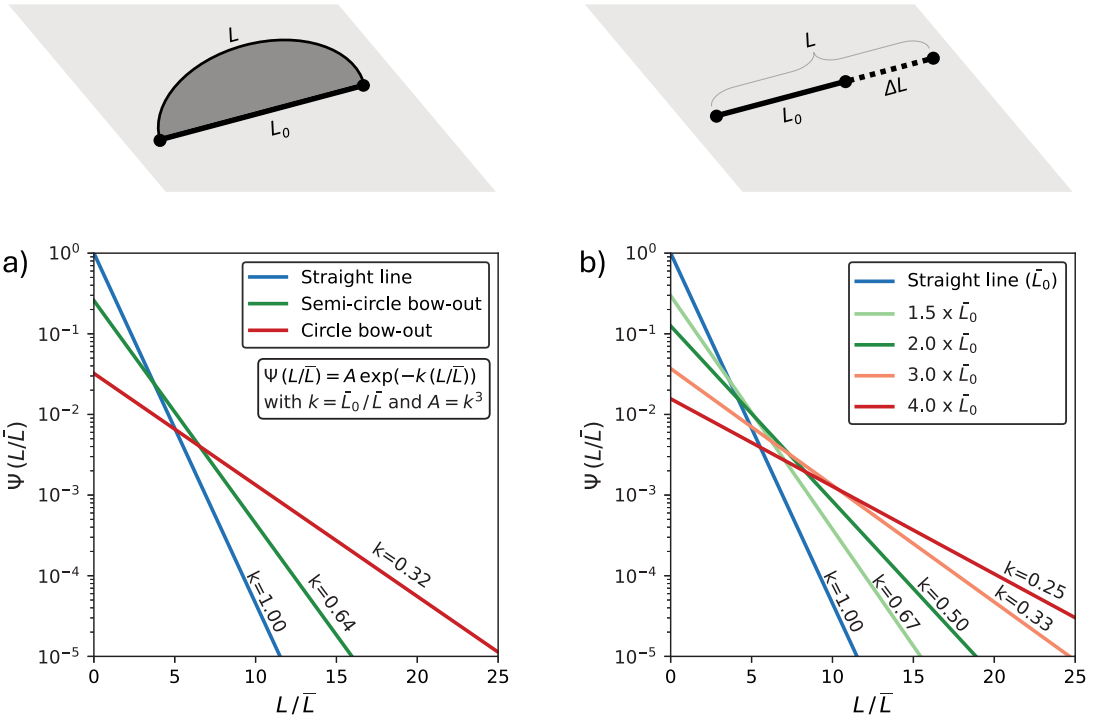

Fig. 19. Dislocation link length distribution modeled by the lengthening due to (a) bow-out and (b) lengthening of dislocation links employing an exponential kernel. The exponent is calculated by $k = \bar{L}_0/\bar{L}$, where $\bar{L}_0$ is the mean initial euclidean distance between the two end nodes of a dislocation link. Panel (a) shows the link lengthening mechanism due to bow-out, whereas panel (b) shows the link lengthening due to the motion of an end node.

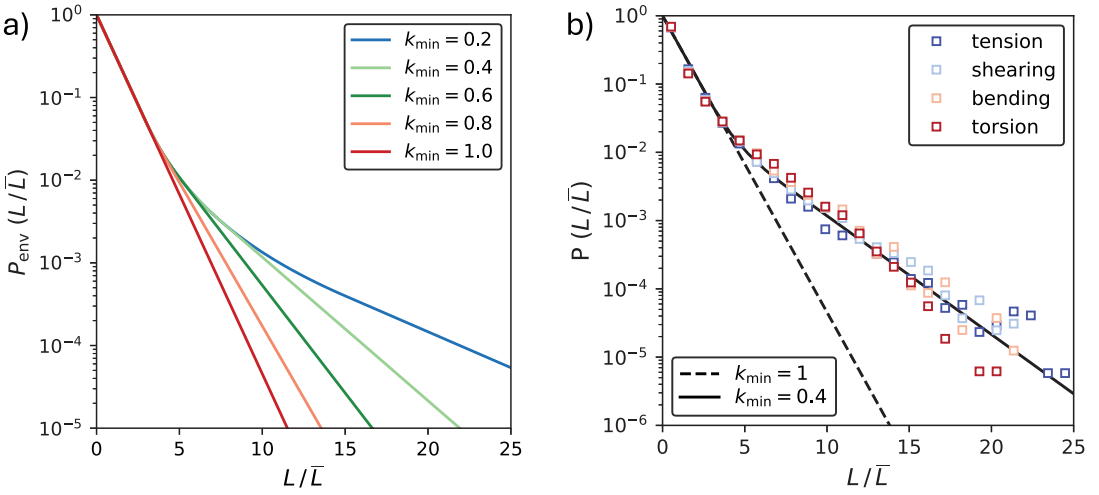

Fig. 20. Exponential envelope probability of dislocation link length distribution for various $k_{\min}$ (a) and applied to the DDD simulation data with $k_{\min} = 0.4$.

For example, double-pinned links (cp. Fig. 6 and Fig. S5) are well described with $k_{\min} = 1$ (no lengthening), whereas semi-pinned and unpinned links require $k_{\min} < 1$, the exact value depending on loading case, e.g. slip system activity.

To derive, whether the bow-out or lengthening mechanism leads to the distinct length distributions for pinning and surface-proximity of dislocation links, we propose the following: If both ends of a dislocation link are pinned, the lengthening mechanism cannot be applied. Additionally, as links barely lengthen for double-pinned links as shown in Fig. 6, the bow-out mechanism

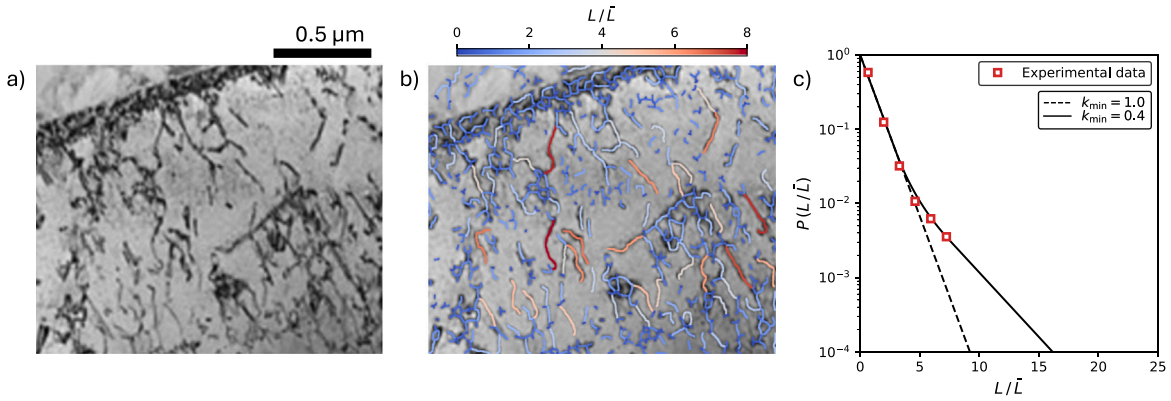

Fig. 21. (a) Experimental TEM image of a fcc metal after plastic deformation with (b) dislocation link extraction of the dislocation network, where the color represents the normalized length of a dislocation link (reprinted and adapted from Gallet et al. (2023) with permission of Elsevier). (c) Link length distribution of the experimental data fitted with $k_{\min} = 0.4$.

has only limited effect on the lengthening. Thus, we suggest that the line tension increment due to pinning of the end nodes is of importance and restricts bow-out of double-pinned dislocation links. Here, dislocation pinning arises naturally from mutual dislocation interactions especially due to a combination of at least two subsequent dislocation reactions (Senger et al., 2011a) shown in Section 3.3 involving three glide planes. However, the observed limitation of dislocation link lengthening due to pinning can also be viewed in a broader context, as similar constraints may arise from other microstructural obstacles such as heterogeneous local microstructures, interfaces of polycrystalline metals or precipitates (McElfresh et al., 2021; Li et al., 2023). Thus, dislocation multiplication is majorly driven by unpinned and semi-pinned dislocation links. We assume that long dislocations act as a main driver for plasticity and for the generation of new dislocation sources due to their low line tension ($\tau_{act} \propto 1/L$), and short links act as stabilizers of the dislocation network and limit the dislocation motion due to pinning. As we carry out simulations with free surfaces, we observed that dislocation links near the surface are contributing more to dislocation link lengthening than dislocation links inside the bulk volume as shown in Fig. 7. This lengthening approach has been considered in the source model (see Section 4), where links bow-out and lengthen if their line tension is exceeded by the local resolved shear stress. Similar conclusions have been observed for dislocation networks with periodic boundary conditions (Akhondzadeh et al., 2026). In addition, we assume that the emergence of the long link length tail may be attributed to the reduced restoring back stress scaling approximately as well with $1/L$, which enables sufficiently long dislocation links to become stabilized within favorable local stress-field minima and network configurations, whereas shorter links tend to retract due to their larger line tension restoring forces. Thus, even in loading scenarios with lower strain rates, we expect that long dislocation links are trapped in dislocation networks although the quantitative scaling of the exponential might be slightly affected (Zhang and Sills, 2024).

To verify experimental evidence of the extended link length distribution, we analyzed the link length distribution from a transmission electron microscopy (TEM) micrograph of a plastically deformed fcc metal. Fig. 21(a) shows a TEM micrograph of 10% strained austenite (Gallet et al., 2023). In (b), image segmentation analysis using OpenCV (Bradski, 2000) was applied to isolate individual dislocation links by skeletonization and connected-component analysis enabling extraction of the corresponding link lengths. The dislocation network contains both short, highly connected and comparatively long dislocation links spanning less obstructed regions. The extracted link length distribution in (c) exhibits an extended long-link tail with $k_{\min} = 0.4$, consistent with the trends observed in the DDD simulations. The coexistence of short links and extended dislocation links further indicates that the evolving dislocation network retains a heterogeneous topology.

To elucidate the role of cross-slip and assess the transferability of the present results to other fcc materials with lower cross-slip probability, we performed additional simulations in which cross-slip was suppressed shown in Appendix I. For the ⟨001⟩ crystal orientation shown in Fig. I.1, simulations performed with and without cross-slip exhibit only minor differences in the mechanical response and link length distribution, indicating a weak sensitivity to cross-slip, although the dislocation multiplication rate is larger for specimens with cross-slip. In contrast, for the ⟨123⟩ crystal orientation in Fig. S12, cross-slip has a more pronounced effect, resulting in higher flow stresses and a higher probability of long link lengths reflected by a lower envelope parameter $k_{\min}$ for specimens with cross-slip. Nevertheless, both with and without cross-slip, the link length distributions exhibit a similar envelope at large link lengths indicating that the formation of long dislocation links is not primarily controlled by the cross-slip probability.

Finally, to demonstrate the strong "natural" convergence towards an exponential envelope distribution, a tensile test with an initial microstructure consisting of prismatic loops with a dislocation length $0.2\,\mu\text{m} \leq L \leq 0.4\,\mu\text{m}$ as shown in Fig. 22(a) is simulated. This initial configuration provides a very narrow-banded initial link length distribution as shown in (c) for $\varepsilon = 0.0\%$. During straining, the exponential envelope distribution naturally forms with the onset of plasticity at $\varepsilon = 0.1\%$ and generates even longer links with ongoing plasticity at $\varepsilon = 0.6\%$ (see also 3D visualization in Fig. 22(b) and link length distribution in (c)). Fig. 22(d) displays the mechanical response of the pristine specimen containing initial prismatic loops, which exhibits a markedly high yield stress. This

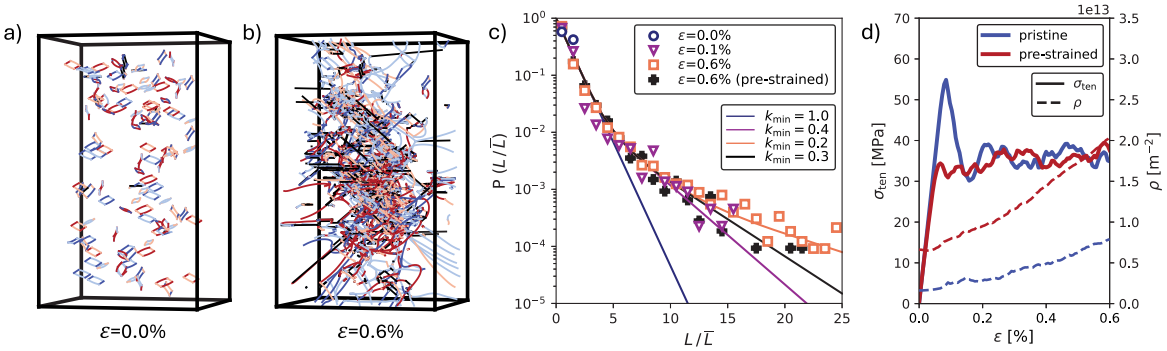

Fig. 22. Convergence to an exponential envelope distribution for initial prismatic loop configuration. The initial dislocation microstructure consisting of prismatic loops (a) and the deformed microstructure at $\varepsilon = 0.6\%$ (b). The link length distribution converges to an exponential envelope probability (c) for a pristine sample. The stress and dislocation density evolution for a pristine as well as a pre-strained prismatic loops microstructure (d).

high stress is expected since initial prismatic link lengths are smaller than $1/\sqrt{\rho_0} \approx 0.5\,\mu\text{m}$. Due to the shorter link length, the resolved shear stress required to bow out and lengthen a dislocation link must exceed the line tension of the $0.4\,\mu\text{m}$ link length, which is at least 25% larger than $1/\sqrt{\rho_0}$. For completeness, we conducted pre-straining for this sample. The treatment increased the initial dislocation density and eliminated the artificial high-yield-stress artifact.

5.2. Origin of mechanical response due to pre-straining

In this study, the effect of pre-straining on the plastic response of single-crystalline metals was examined. The results indicate that pre-straining with an associated strain path change leads to higher flow stresses under tensile loading for both ⟨001⟩ and ⟨123⟩ crystal orientations. Previous studies have reported both a reduction (Lee et al., 2009; El-Awady et al., 2013; El-Awady, 2015) and an increase (Schneider et al., 2013) in flow stress for pre-strained samples under homogeneous loading conditions. These apparently contradictory observations can be interpreted in terms of the size-dependent parameter $t\sqrt{\rho}$, which combines the specimen thickness t and the dislocation density ρ (El-Awady, 2015). For small values of $t\sqrt{\rho}$, which is characteristic for small specimens or low dislocation densities, plastic deformation is controlled by a small number of pre-existing dislocation links. In this regime, pre-straining introduces additional mobile dislocations contributing to plasticity and leading to a reduction of the flow stress. In contrast, for larger values of $t\sqrt{\rho}$, which is characteristic for larger specimens or higher dislocation densities, the flow stress is primarily governed by dislocation forest interactions. An increase in dislocation density therefore strengthens the dislocation network and results in higher flow stresses.

Within this framework, the present study falls within a comparatively larger $t\sqrt{\rho}$ regime than several previous DDD investigations (El-Awady et al., 2013; El-Awady, 2015; Song et al., 2019), which explains the observed increase in flow stress after pre-straining during tensile loading. Shearing along the ⟨001⟩ crystal orientation exhibits only a marginal increase in flow stress after pre-straining, in contrast to the ⟨123⟩ crystal orientation. This behavior may be attributed to the fact that the slip systems that become dominant during subsequent shearing were inactive during pre-straining (cp. Fig. F.1). As a result, the dislocation network undergoes a reorganization during the change in loading path leading to a modified flow response despite the increased initial dislocation density. A systematic investigation of different pre-strain directions and loading-path changes remains the subject of further studies. Interestingly, the opposite trend is observed for gradient-imposed loading conditions such as bending and torsion, where the flow stress decreases after pre-straining. Deformation under strain gradients is strongly influenced by dislocation pile-ups, which generate significant back stresses (Motz et al., 2008). The simulations indicate that extended pile-ups occur more frequently in specimens with smaller $t\sqrt{\rho}$. Consequently, pristine samples with lower initial dislocation densities exhibit more pronounced pile-up formation compared to pre-strained samples resulting in higher flow stresses. We note that the negative hardening rate observed for torsion loading of the pre-strained samples in the ⟨001⟩ crystal orientation may be attributed to the relatively early deformation stage at approximately 0.8° and could evolve into positive hardening at larger deformations.

5.3. Origin of enhanced and suppressed dislocation multiplication due to pre-straining

In this study, we observe enhanced and suppressed dislocation multiplication for tensile loading in ⟨001⟩ crystal orientation due to pre-straining and the associated strain path change as shown in Fig. 12. In general, dislocation multiplication and plastic shear is dominated by eight active slip systems with a Schmid factor of $S^{\xi} = 0.41$. However, we observe that dislocation multiplication is strongly influenced by the dislocation network developed during pre-straining leading to either enhanced and suppressed dislocation multiplication on specific slip system groups detailed later. These differences can be attributed to three factors: for

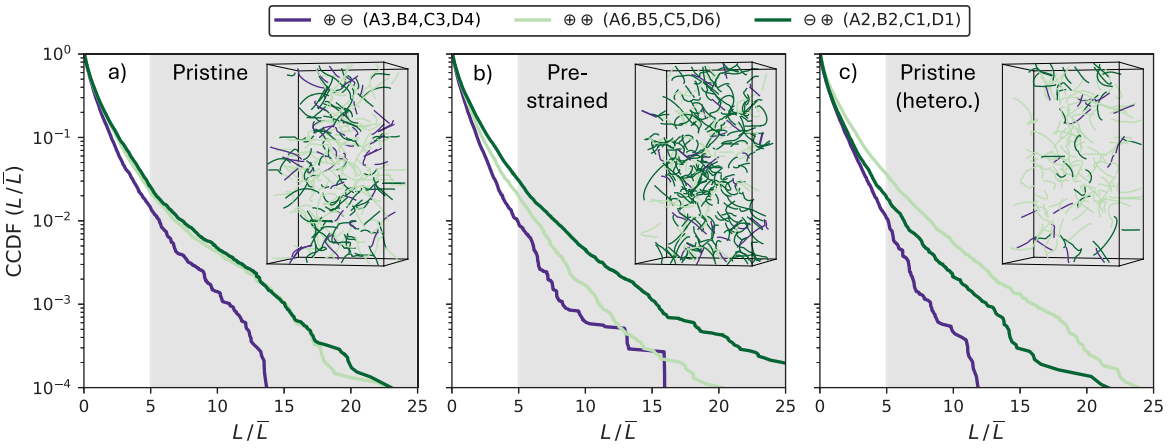

Fig. 23. CCDF of dislocation link lengths for (a) pristine, (b) pre-strained and (c) heterogeneous pristine samples at $\varepsilon = 0.6\%$. The color coding refers to the three distinct slip system groups derived from the strain path change of the pre-strained sample and the inset shows the 3D dislocation networks for dislocation links with $L/\bar{L} \geq 5$ (indicated by the gray background).

one, a heterogeneous dislocation density distribution per slip system, second, the heterogeneous junction formation hindering links to multiply on specific slip systems, and third the dislocation network characteristics such as link lengthening and pinning.

To distinguish between enhanced and suppressed plasticity, we classify the slip systems into three groups based on the strain-path change of the pre-strained sample, which is first pre-strained along ⟨100⟩, then relaxed, and subsequently loaded in tension along the ⟨001⟩ direction (Table 1). This leads to the slip system group ⊕⊕ (A6, B5, C5, C6), with active slip systems active during both pre-straining and subsequent tension, to group ⊖⊕ (A2, B2, C1, D1), in-active during pre-straining but active during subsequent tension, and to group ⊕⊖ (A3, B4, C3, D4), active for pre-straining but inactive during subsequent tension.

Fig. 23 shows that the CCDF of the groups ⊖⊕ and ⊕⊕ in the pristine sample are similar (a) as expected based on the Schmid factors (cp. Table 1), whereas the ⊖⊕ group has a larger CCDF than the group ⊕⊕ for the pre-strained sample (b). The insets reveal visual differences in the dislocation network for links with $L/\bar{L} \geq 5$. To elucidate the effect of initially heterogeneous dislocation density fractions per slip system as observed for the pre-strained sample, a tensile test for an additional pristine sample with initially heterogeneous dislocation density ratios and homogeneous junction distributions (pristine hetero.) is performed. The sample is generated by relaxation of dislocation loops (cp. Appendix A) initially seeded with heterogeneous fractions per slip system to mimic the $\rho^{\xi}/\rho_{\text{tot}}$ of the pre-strained sample. The result CCDF reveals larger link lengths for ⊕⊕ than for the ⊖⊕ group (cp. Fig. 23(c)). As expected, the ⊕⊖ group shows barely any link lengthening for all three specimens as those slip systems have Schmid factor zero during tensile loading.

The contribution of the slip system groups to plasticity of these three samples is shown in Fig. 24. In the pristine sample, the ⊖⊕ and the ⊕⊕ group contribute similarly to plastic slip (b) and dislocation multiplication (d). In contrast, in the pre-strained sample, plasticity is dominated by ⊖⊕, and in the heterogeneous pristine sample by the ⊕⊕ group. For all three samples, the ⊕⊖ group does not contribute to plasticity. Thus, plasticity directly correlates with the largest long tail of the CCDF for dislocation link lengths (Fig. 23). Although the total dislocation density evolution (c), which correlates with the flow stress (a), seems not to be directly affected by the enhanced and suppressed plasticity, microstructural differences are significant, which is why the identified origins are examined in the following:

First, enhanced and suppressed dislocation multiplication can originate from initially heterogeneous dislocation density fractions per slip system (cp. Figs. 23 and 24). This originates from an increasing likelihood of link lengthening on the initially higher populated slip systems of the ⊕⊕ group.

Second, dislocation junctions due to pre-straining contribute to the enhanced and suppressed dislocation multiplication (Fig. 11(b)). Due to a larger amount of double-pinned junctions as well as due to the lower amount of Lomer and collinear junctions on the ⊖⊕ group, we suppose that dislocation motion significantly differs due to the heterogeneous junction forest (Franciosi et al., 1980), e.g. influenced by collinear junctions (Madec et al., 2003), modifying the mean free paths (Devincre et al., 2008). Thus, for crystal plasticity, junction density evolution is of great importance (Roters et al., 2019; Sudmanns et al., 2020; Katzer et al., 2024b).

Third, the link length distribution and pinning affect the dislocation multiplication. Pinning of dislocation links hinders link lengthening and therefore suppresses dislocation multiplication (Fig. 6). The strain path change for pre-strained samples increases the variety of pinning mechanisms (Fig. 9) and therefore the likelihood of pinning due to successive activations within the ⊕⊕ group. And although the initial fraction of pinned dislocation links is larger on the ⊖⊕ group generated passively by being an obstacle for activated links (Fig. 11), the likelihood of new pinning during subsequent loading is larger for the ⊕⊕ than for the ⊖⊕ group as those links are active during both steps. This leads to distinct differences in pinning fractions on the slip systems as shown in Appendix H. Therefore, pinning mainly contributes to the distinct link length differences for the pre-strained as well as the heterogeneous

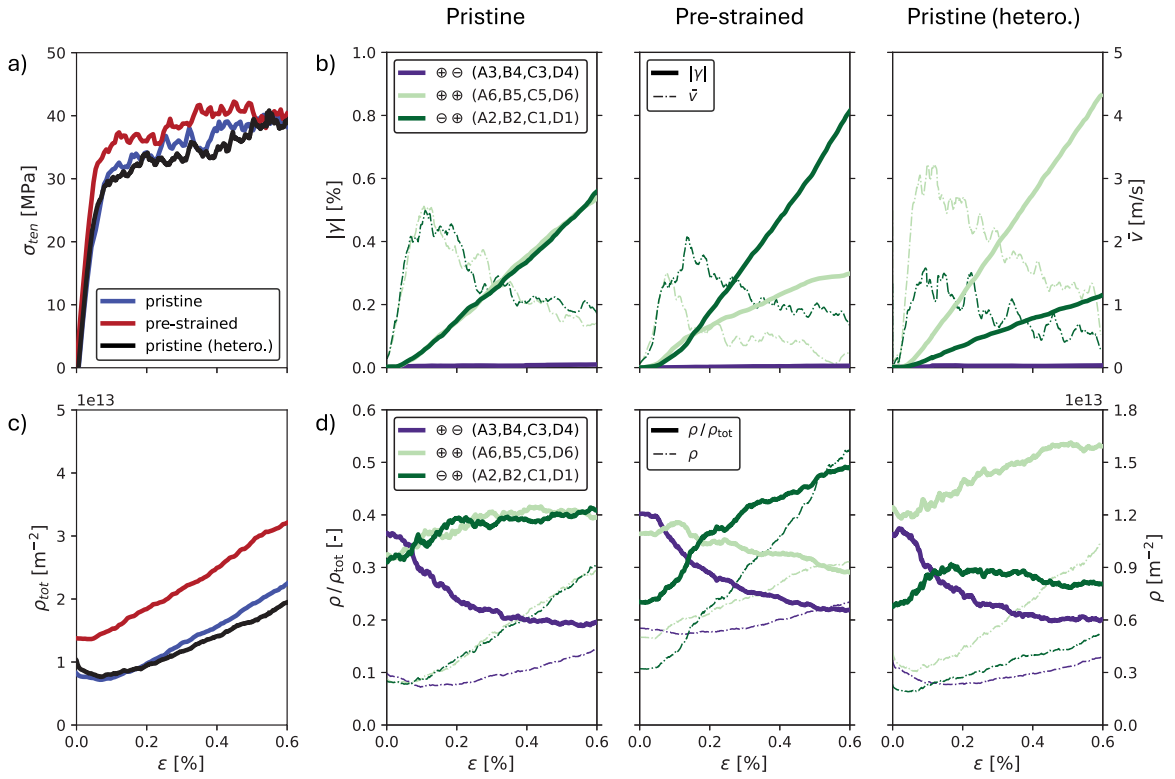

Fig. 24. The effect of pre-straining and heterogeneous dislocation density distributions in ⟨001⟩ crystal orientation in tension. Panel (a) shows the tensile stress and (c) the dislocation density evolution during straining. Panel (b) shows the absolute plastic strain $|\gamma|$ and mean velocity $\bar{v} = \Delta\gamma/(\Delta t\, b\, \rho)$ and (d) the fraction ρ/ρ_{tot} and ρ for the three distinct slip system groups (⊕⊖, ⊕⊕, ⊖⊕) derived from the strain path change due to pre-straining.

pristine sample (Fig. 23) contributing to enhanced and suppressed plasticity. We note that the observed mechanisms extend similar observations of pinning such as a combined glissile and cross-slip mechanism (Wang et al., 2024), which is also observed here, leading to the formation of a spiral source (Motz et al., 2009). Furthermore, we emphasize that these interaction sequences are different to binary dislocation junction mechanisms or mechanisms combining e.g. glissile and coplanar reactions (Akhondzadeh et al., 2021) as the end nodes are unpinned and still able to move along the intersection line of the two involved slip systems planes. In addition, the occurrence of enhanced pinning of dislocation links due pre-straining has been experimentally observed leading to enhanced subsequent plastic deformation (Li et al., 2023).

5.4. Continuum plasticity model based on statistical features

The probabilistic dislocation-based plasticity model developed in this work shows that based, by incorporating statistical characteristics of dislocation networks, it is possible to predict dislocation multiplication, plastic shear strain and the resulting mechanical response (Figs. 14, 16 and 17). In particular, the model formulation emphasizes the role of the link-length probability distribution $P(L/\bar{L})$, which implicitly captures the statistical consequences of dislocation reactions on the topology evolution without explicitly resolving these mechanisms. The evolving statistics are reflected by the envelope distribution $P_{\text{env}}(L/\bar{L})$, towards which dislocation networks "naturally" converge, including pristine, pre-strained and strongly skewed initial configurations with prismatic loops (Figs. 20 and 22). Beyond static characteristics, the model also incorporates temporal characteristics through the link lifetime distributions $P(T_{\text{src}})$ and $P(T_{\text{surf}})$, which determine how long links remain active and thus influence plastic deformation. Take together, the link-length and link activation period distributions provide a probabilistic description of both structural and temporal aspects of dislocation plasticity.

To generate plasticity in the proposed model, dislocation sources are activated when the resolved shear stress exceeds a critical source stress (cp. Eq. (5)), which incorporates both link length and pinning. The pinning characteristic β_j is currently assigned based on qualitative assumptions that reflect the different likelihoods of source activation for the pinning types. In particular, unpinned links are assumed to be more likely to act as a source than semi-pinned and double-pinned links. While this assumption provides a simple statistical representation of source activation, it does not explicitly account for the underlying physical mechanisms governing

source formation and activation. Therefore, it would be of interest to investigate how the activation probability depends on pinning with respect to the yield stress (Ispánovity et al., 2014), in order to incorporate pinning effects into continuum modeling (Hunter and Preston, 2015). In addition, the duration of an activated source is currently approximated using a characteristic source activation time drawn from the distribution $P(T_{\mathrm{src}})$. This time scale is derived from our DDD simulations, and although length and time scales in dislocation plasticity can be correlated (Berta et al., 2025b), we deliberately treat the time scale as a probabilistic uncorrelated feature to assess how universal the static and temporal characteristics of the dislocation network are.

Despite these simplifications, the predicted mechanical response remains accurate and captures size effects (Fig. 17), including discrete step-like features similar to dislocation avalanches observed experimentally (Ispánovity et al., 2022; Berta et al., 2025a). These intermittent events are particularly prominent in small specimens with a size of 1 μm, where plastic deformation is governed by the activation and motion of only a few dislocation links. With increasing specimen size, stress drops become less frequent as multiple dislocation links are activated simultaneously, resulting in a more collective dislocation motion. This transition from discrete to more continuous plastic flow is captured by the probabilistic model, as illustrated for the 5 μm specimen. In addition, when considering multiple model realizations (Fig. 18), the model uncertainty decreases with increasing specimen size reflecting the transition to bulk behavior. The generated slip system dependent plasticity agrees well with DDD predictions (Fig. 15). However, some deviations occur, as dislocation multiplication is overestimated on active and underestimated on inactive slip systems due to the absence of dislocation density transfer between systems via glissile, coplanar or cross-slip reactions. Thus, a limitation of the present formulation is that it represents dislocation networks primarily through statistical descriptors, while dynamic topology changes are only incorporated implicitly through the evolution of the link-length distribution. For broader applicability, the model could be extended by introducing dislocation density transfer terms that account for specific reaction mechanisms through reaction type dependent rate formulations (Katzer et al., 2022).

Previous studies have demonstrated that incorporating link length distributions into finite-strain crystal plasticity frameworks enables the prediction of the mechanical response of fcc metals over a broad range of temperatures and strain rates (Ye et al., 2023a,b). In these approaches, the long link length tail of the distribution is used to estimate the fraction of mobile dislocation density, which subsequently governs the dislocation density evolution. In contrast, the present framework does not explicitly distinguish between mobile and immobile dislocation densities. Instead, dislocation link lengths, spatial positions and reaction frequencies are sampled probabilistically from distributions directly extracted from DDD simulations, while additionally accounting for physical mechanisms such as surface proximity and pinning. Thus, this model description enables the prediction of bulk material behavior in large-scale specimens as well as of intermittent plasticity phenomena such as dislocation avalanches in small-scale specimens extending approaches like time-discontinuous frameworks (Lamari et al., 2025).

Overall, the present results underscore the importance of statistical dislocation network descriptors for continuum modeling and demonstrate that probabilistic approaches can provide an efficient bridge between discrete dislocation dynamics and continuum plasticity models, in line with other scale-bridging methodologies (Tan et al., 2021; Ruestes and Segurado, 2024; Hunter et al., 2026) as well as combining with experimental observations (Papanikolaou et al., 2017; Gallet et al., 2023; Hunter et al., 2026).

6. Conclusion

In this study, dislocation networks of fcc Aluminum single crystals were characterized under varying boundary conditions using three-dimensional discrete dislocation dynamics (DDD) simulations demonstrating how dislocation link lengths evolve due to the processes of gliding, entanglement and pinning. More than hundred DDD simulations were performed under homogeneous (tension, shear) and gradient-induced (bending, torsion) boundary conditions for both relaxed and pre-strained dislocation networks. Based on derived representative dislocation network characteristics, a probabilistic dislocation-based plasticity model was developed to bridge the discrete scale and the continuum regime demonstrating high predictive accuracy of plastic deformation processes. The following conclusions can be drawn:

- Dislocation networks reveal boundary condition independent characteristics such as the dislocation link length distribution $P(L/\bar{L})$ for which a naturally evolving distribution function is derived based on bow-out and link lengthening. In addition, pinning mechanisms and their effect of suppressing the long tail of link length distributions are revealed.
- The probabilistic dislocation-based plasticity model reveals high predictive accuracy of dislocation multiplication, plastic shear and mechanical response by incorporating static features such as the link length distribution, pinning and surface proximity, as well as dynamic features such as dislocation reaction frequencies. In addition, the proposed model demonstrates predictive capability across different specimen sizes naturally capturing the resulting size effects.
- Pre-straining of dislocation network reveals previously unreported enhanced and suppressed dislocation multiplication and plastic shear due to an increased number of dislocation junctions, redistribution of dislocation density, a shifted long tail of dislocation link lengths and enhanced dislocation link pinning.

Overall, these findings provide important ingredients for the development of physically informed, dislocation-based constitutive theories of plasticity, emphasizing how dislocation network characteristics are represented at the coarse-grained level in continuum frameworks such as continuum dislocation dynamics (CDD) or crystal plasticity (CP).

CRediT authorship contribution statement

Balduin Katzer: Writing – review & editing, Writing – original draft, Visualization, Validation, Software, Methodology, Investigation, Formal analysis, Data curation, Conceptualization. **Daniel Weygand:** Writing – review & editing, Writing – original draft, Validation, Supervision, Software, Methodology, Funding acquisition, Conceptualization. **Katrin Schulz:** Writing – review & editing, Writing – original draft, Supervision, Project administration, Funding acquisition, Conceptualization.

Declaration of competing interest

The authors declare that they have no known competing financial interests or personal relationships that could have appeared to influence the work reported in this paper.

Acknowledgments

We gratefully acknowledge the financial support of this work in the context of the German Research Foundation (DFG) project SCHU 3074/4-1 and the funding by the Carl-Zeiss-Stiftung, Germany. The simulations were performed on the HoreKa supercomputer funded by the Ministry of Science, Research and the Arts Baden-Württemberg and by the Federal Ministry of Education and Research, Germany. The authors acknowledge support by the state of Baden-Württemberg through bwHPC.

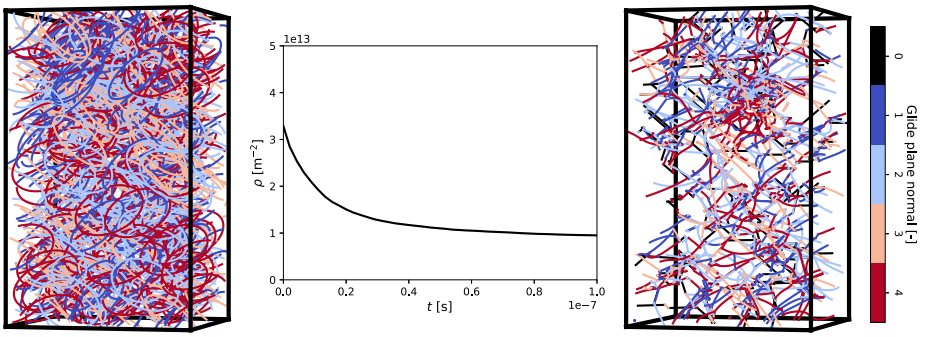

Fig. A.1. Relaxation of circular dislocation loops (left) leading to a relaxed dislocation network (right), where the color coding indicates the slip plane normal and 0 represents physical dislocation junctions. The dislocation density decreases during relaxation (center).

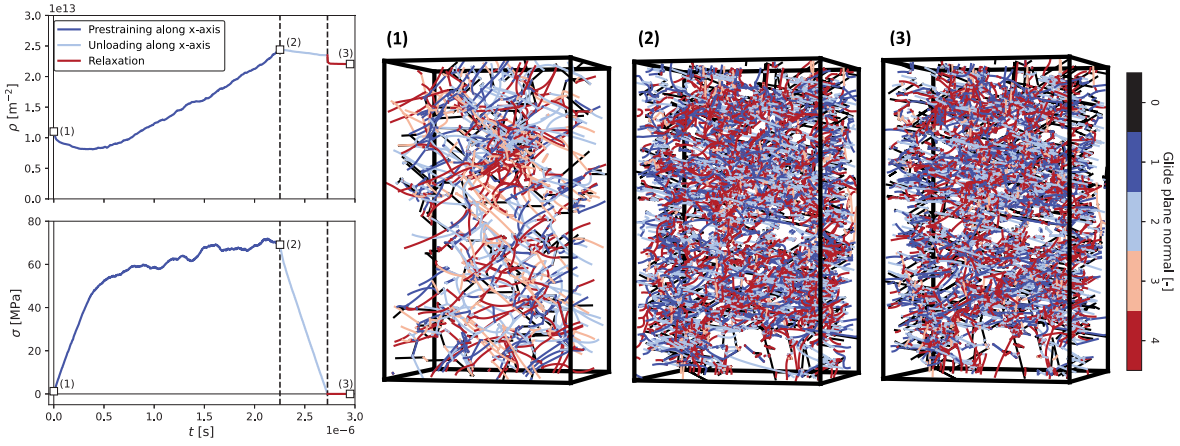

Fig. B.1. Pre-straining procedure of dislocation networks. On the left, the evolution of dislocation density and stress over time is shown for the entire procedure including pre-straining, unloading and relaxation. The numbers within the curves refer to the dislocation network snapshots on the right indicating the initial state (1), the state during pre-straining (2) and the final state after unloading and subsequent relaxation (3). The color coding of the dislocation networks indicates the slip plane normal.

Appendix A. Relaxation procedure

The goal of the relaxation procedure is to achieve a quasi-equilibrium state where dislocations are configured in a stable network, reflecting more accurately a real initial dislocation structure prior straining (Motz et al., 2009). The relaxation procedure is illustrated in Fig. A.1. Starting with N circular dislocation loops with a radius r of size $0.2\,\mu\text{m} - 1.0\,\mu\text{m}$ which are randomly seeded within the specimen, the dislocation configuration is relaxed under traction free boundary conditions on the samples surface using the standard DDD time evolution scheme. The quasi-equilibrium state is reached when the dislocation density ρ keeps constant.

Appendix B. Pre-straining procedure

Pre-straining is employed to generate network heterogeneity, which is depicted in Fig. B.1. Thereby, the initial dislocation network (1) is pre-strained along the x-axis with a constant strain rate $\dot{\varepsilon}$ of 2000 s^{-1}. The evolution of dislocation density as well as stress is shown on the left. After reaching a total strain ε of $\approx 0.5\%$ (2), the specimen is unloaded until zero stress is reached (cp. the decrease of the stress-time curve). Subsequently a relaxation procedure is applied to achieve a quasi-equilibrium state (cp. the small dislocation density drop in the dislocation density-time curve). This results in the final pre-strained configuration (3), which is used as initial structure for analyzing network heterogeneity upon further loading.

Appendix C. Schmid factor for boundary conditions

The Schmid factors are calculated from a normalization of Eq. (4) using

$$S^{\xi} = 1/\tau_{\text{ext}}\, \mathbf{M}^{\xi} \cdot \boldsymbol{\sigma}_{\text{ext}}.$$

The stress fields for the different boundary conditions can be written as follows. For tension, the stress field is calculated by $\boldsymbol{\sigma}_{\text{ext}} = \tau_{\text{ext}}\, \mathbf{e}_y \otimes \mathbf{e}_y$. Pure bending can be decomposed into a tension and a compression regime leading to the same Schmid factors as for tension however with both positive and negative signs. For simple shear, a uniform shear stress $\boldsymbol{\sigma}_{\text{ext}} = \tau_{\text{ext}} \left(\mathbf{e}_x \otimes \mathbf{e}_y + \mathbf{e}_y \otimes \mathbf{e}_x\right)$ is applied. For torsion, $\boldsymbol{\sigma}_{\text{ext}}(r,\phi) = \tau_{\text{ext}}(r) \left(\mathbf{e}_\phi \otimes \mathbf{e}_y + \mathbf{e}_y \otimes \mathbf{e}_\phi\right)$ with $\mathbf{e}_\phi = \cos\phi\, \mathbf{e}_x - \sin\phi\, \mathbf{e}_z$ is considered. The maximum Schmid factor for a slip system is determined by maximizing the magnitude of the resolved shear stress with respect to ϕ. The maximum Schmid factor S^{ξ}_{max} is therefore defined as the maximum over all possible angles $\phi \in [0, 2\pi)$. The corresponding angle ϕ^{ξ}_{max} is the orientation at which S^{ξ}_{max} is reached.

Appendix D. Dislocation density evolution

The dislocation density evolution for each considered loading condition is shown in Fig. D.1 for specimens with a $\langle 001 \rangle$ crystal orientation. Pristine samples have initial dislocation densities of $\rho \approx 10^{13}$ m^{-2}, whereas pre-strained samples have larger densities of $\rho \approx 2 \cdot 10^{13}$ m^{-2}. The dislocation multiplication rate is resembling between pristine and pre-strained samples for each loading condition. However, pre-strained samples do not exhibit initial dislocation density decrease compared to pristine samples at the onset of loading.

Appendix E. Dislocation reaction rate

Fig. E.1 shows the probability distributions of the reaction frequency ν_{src} for the four different boundary conditions (tension, shearing, bending, and torsion) in the two crystal orientations (a) $\langle 001 \rangle$ and (b) $\langle 123 \rangle$. The reaction frequency is estimated by the characteristic activation period $\nu_{\text{src}} = 1/T_{\text{src}}$, which is calculated as $\nu_{\text{src}} = \Delta n_{reac}/(n_{links}\,\Delta \text{t})$ for a time step Δt, where n_{reac} represents the number of all dislocation physical and virtual junctions and n_{links} the number of all dislocation links. In both orientations, tension, shearing, and bending exhibit relatively similar distributions concentrated at lower ν_{src} values with $\approx 1.0\,\text{MHz}$, whereas torsion displays a markedly broader distribution shifted towards higher frequencies with a mean frequency of $\approx 2.5\,\text{MHz}$. Overall, the results demonstrate that the reaction frequency ν_{src} depends predominantly on the applied loading scenario rather than the crystal orientation. Fig. E.1(c) shows that the reaction frequency varies between the considered specimen sizes, with lower frequencies for 1μm samples and larger frequencies for 5μm samples.

$$f(\nu_{\text{src}}) = \frac{1}{s_{\nu_{\text{src}}}\sqrt{2\pi}} \exp\left(-\frac{\left(\nu_{\text{src}} - \bar{\nu}_{\text{src}}\right)^2}{2 s^2_{\nu_{\text{src}}}}\right), \tag{E.1}$$

where $\bar{\nu}_{\text{src}}$ denotes the mean source frequency and $s_{\nu_{\text{src}}}$ represents the standard deviation. In addition, we observe that the distributions tend to collapse onto a common curve when considering the size-dependent parameter $t\sqrt{\rho}$ with thickness t and dislocation density ρ as shown in the inset of Fig. E.1(c).

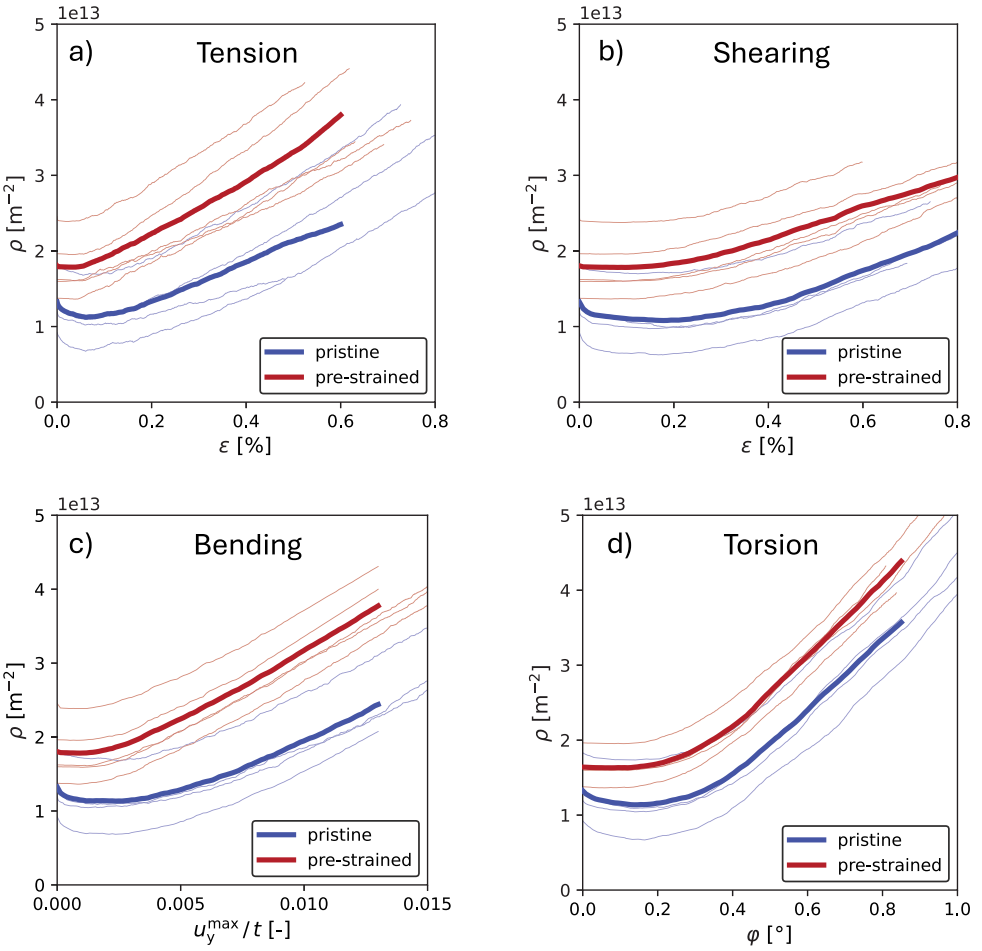

Fig. D.1. Dislocation density evolution for (a) tension, (b) shearing, (c) bending and (d) torsion in ⟨001⟩ crystal orientation.

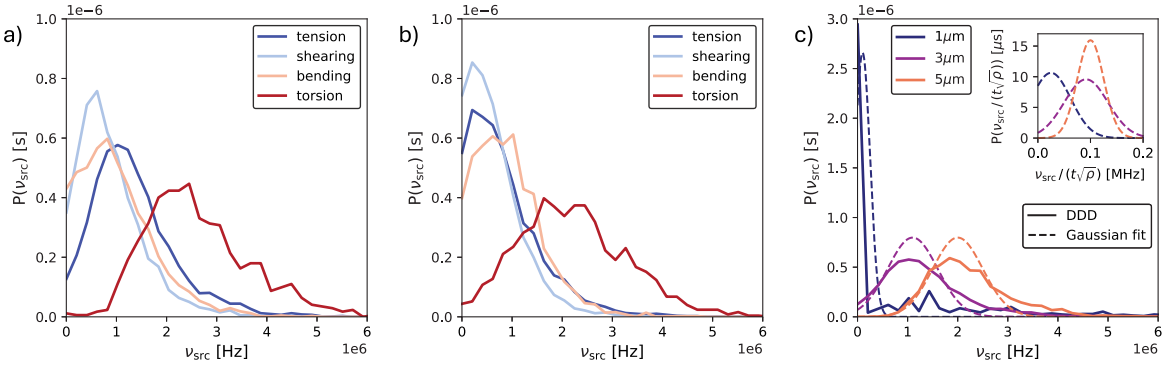

Fig. E.1. The reaction frequency ν_{src} for tension, shearing, bending and torsion (a) in ⟨001⟩ crystal orientation and (b) in ⟨123⟩ crystal orientation. Panel (c) shows the reaction frequency for 1 μm, 3 μm and 5 μm samples for tension as well as the employed Gaussian fit. The inset shows the dependency of the reaction frequency on $t\sqrt{\rho}$ with thickness t and dislocation density ρ.

Appendix F. Pre-strain effect on subsequent shearing, bending and torsion

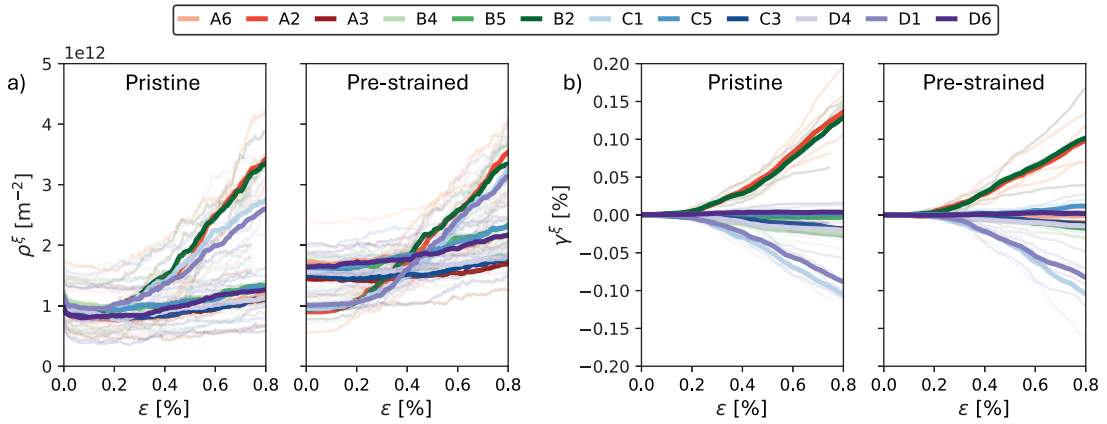

Fig. F.1. The effect of pre-straining for shearing in ⟨001⟩ crystal orientation on the evolution of (a) dislocation density ρ^ξ and (b) plastic shear γ^ξ per slip system ξ.

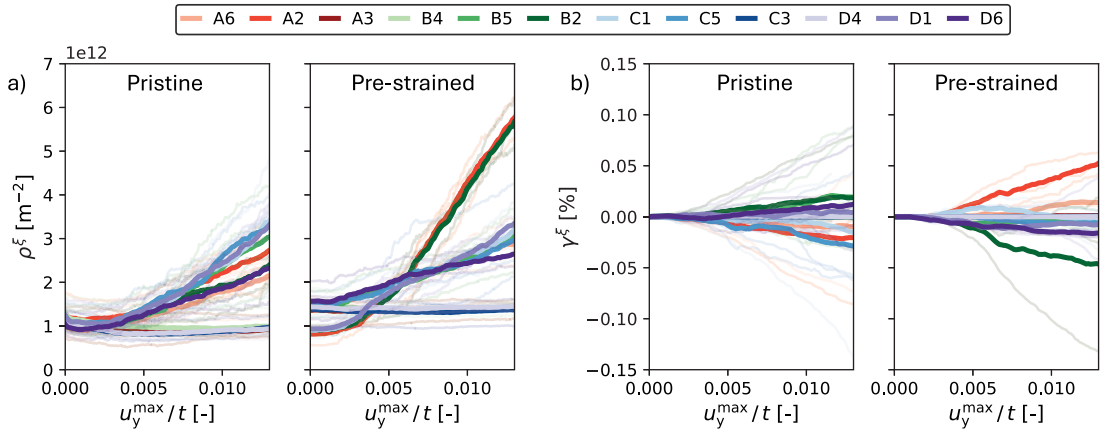

Fig. F.2. The effect of pre-straining for bending in ⟨001⟩ crystal orientation on the evolution of (a) dislocation density ρ^ξ and (b) plastic shear γ^ξ per slip system ξ.

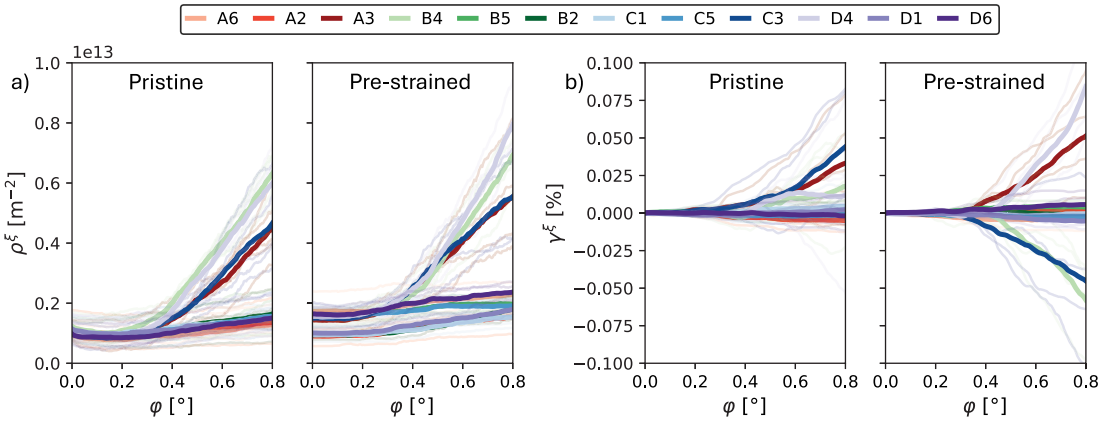

Fig. F.3. The effect of pre-straining for torsion in ⟨001⟩ crystal orientation on the evolution of (a) dislocation density ρ^ξ and (b) plastic shear γ^ξ per slip system ξ.

The evolution of the dislocation density ρ^{ξ} and the plastic shear γ^{ξ} for each slip system ξ is shown for shearing F.1, bending F.2 and torsion F.3 in ⟨001⟩ crystal orientation. Pre-straining leads to initially heterogeneous dislocation density distributions. However, the subsequent dislocation multiplication and plastic shear follows the trends comparable to the pristine samples for shearing. For bending, enhanced and suppressed dislocation multiplication and plastic shear is observed. For torsion, the dislocation multiplication follows the pristine behavior, but the plastic slip differs leading to more plasticity for pre-strained samples. This result indicates that under shearing and torsion there is no enhanced or suppressed dislocation multiplication due to pre-straining, in contrast to the stronger multiplication effects observed in tension and bending.

Appendix G. Derivation of the envelope probability

Let $x := L/\bar{L}$ and consider, for $k \in [k_{\min}, 1]$, the unnormalized exponential kernel

$$\Psi(x,k) = k^3 e^{-kx}, \qquad x \geq 0. \tag{G.1}$$

The exponential envelope kernel over admissible k is

$$\Psi_{\text{env}}(x) = \sup_{k_{\min} \leq k \leq 1} \Psi(x,k) = \sup_{k_{\min} \leq k \leq 1} k^3 e^{-kx}, \qquad x \geq 0. \tag{G.2}$$

For fixed $x \geq 0$, maximize $\Psi(x,k)$ by maximizing its logarithm

$$\ell(k) = \ln\left(k^3 e^{-kx}\right) = 3\ln k - kx, \tag{G.3}$$

which is strictly concave since $\ell''(k) = -3/k^2 < 0$. The first-order condition

$$\ell'(k) = \frac{3}{k} - x = 0 \tag{G.4}$$

yields the unconstrained maximizer $k^*(x) = 3/x$. Imposing $k \in [k_{\min}, 1]$ gives

$$k_{\text{opt}}(x) = \min\left(1, \max\left(k_{\min}, \frac{3}{x}\right)\right). \tag{G.5}$$

Therefore, the exponential envelope kernel admits the closed form

$$\Psi_{\text{env}}(x) = \left(k_{\text{opt}}(x, k_{\min})\right)^3 \exp\left(-x\, k_{\text{opt}}(x, k_{\min})\right), \qquad x \geq 0. \tag{G.6}$$

It first differs from the simple exponential with $k = 1$ when $3/x < 1$, i.e. for $x > 3$. Using the optimizer's piecewise form,

$$k_{\text{opt}}(x) = \begin{cases} 1, & 0 \leq x \leq 3, \\ \dfrac{3}{x}, & 3 < x < \dfrac{3}{k_{\min}}, \\ k_{\min}, & x \geq \dfrac{3}{k_{\min}}, \end{cases} \tag{G.7}$$

we obtain the explicit exponential envelope kernel

$$\Psi_{\text{env}}(x) = \begin{cases} e^{-x}, & 0 \leq x \leq 3, \\ 27\, e^{-3}\, x^{-3}, & 3 < x < \dfrac{3}{k_{\min}}, \\ k_{\min}^3 e^{-k_{\min} x}, & x \geq \dfrac{3}{k_{\min}}. \end{cases} \tag{G.8}$$

To obtain a proper probability density P_{env} on $[0, \infty)$, normalize Ψ_{env} with

$$C = \int_0^{\infty} \Psi_{\text{env}}(x)\, dx = I_1 + I_2 + I_3, \tag{G.9}$$

where

$$\begin{aligned} I_1 &= \int_0^3 e^{-x}\, dx = 1 - e^{-3}, \\ I_2 &= \int_3^{3/k_{\min}} 27 e^{-3} x^{-3}\, dx = \frac{3}{2} e^{-3}\,(1 - k_{\min}^2), \\ I_3 &= \int_{3/k_{\min}}^{\infty} k_{\min}^3 e^{-k_{\min} x}\, dx = k_{\min}^2 e^{-3}. \end{aligned} \tag{G.10}$$

Hence

$$C = 1 - e^{-3} + \frac{3}{2} e^{-3}(1 - k_{\min}^2) + k_{\min}^2 e^{-3} = 1 + \frac{e^{-3}}{2}\left(1 - k_{\min}^2\right). \tag{G.11}$$

Finally, define the normalized exponential envelope probability

$$P_{\text{env}}(x) = \frac{\Psi_{\text{env}}(x)}{C} = \frac{1}{1 + \frac{e^{-3}}{2}(1 - k_{\min}^2)} \left(k_{\text{opt}}(x, k_{\min})\right)^3 \exp\left(-x\, k_{\text{opt}}(x, k_{\min})\right), \qquad x \geq 0. \tag{G.12}$$

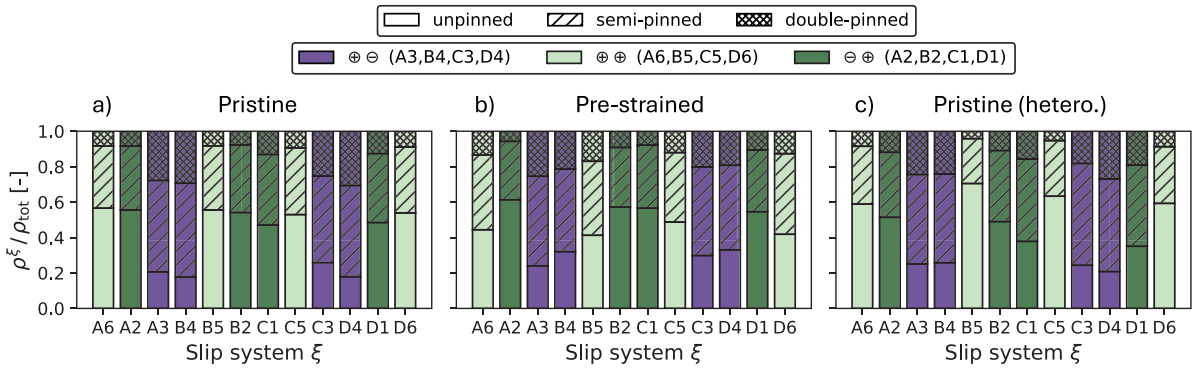

Fig. H.1. Fractions of unpinned, semi-pinned and double pinned dislocation links for (a) pristine, (b) pre-strained and (c) heterogeneous pristine samples at $\epsilon = 0.6\%$. The color coding refers to the three distinct slip system groups derived from the strain path change of the pre-strained sample.

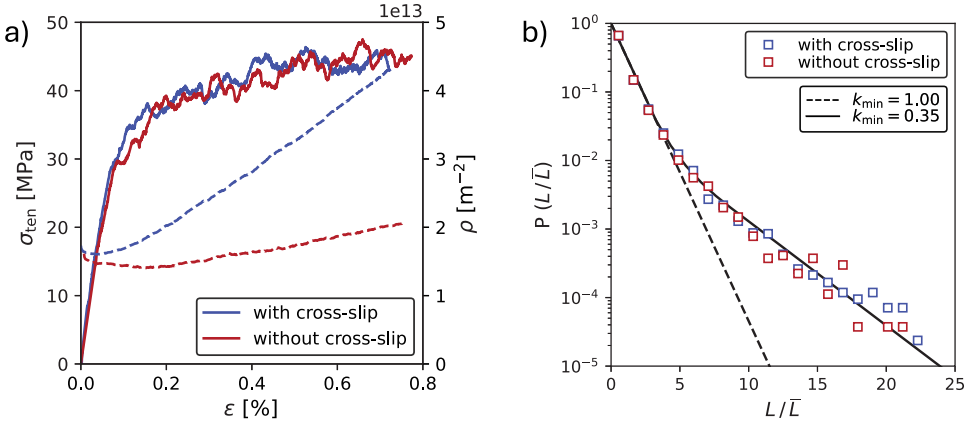

Fig. I.1. Dislocation network evolution with and without cross-slip in ⟨001⟩ crystal orientation. (a) The mechanical response and the dislocation density evolution. (b) The link length distribution at $\epsilon = 0.6$ with an envelope of $k_{min} = 0.35$ for both scenarios.

Appendix H. Pinning of dislocation links due to pre-straining

Fig. H.1 compares the normalized dislocation density fractions ρ^ξ/ρ_{tot} per slip system ξ for the (a) pristine, (b) pre-strained and (c) heterogeneous pristine samples. In the pristine state (a), the slip systems exhibit nearly uniform fractions of unpinned, semi-pinned and double-pinned links across each slip system group ⊖⊕, ⊕⊕ and ⊕⊖. After pre-straining (b), pronounced differences emerge as the ⊖⊕ group shows a marked increase in pinned segments compared to the ⊕⊕ group. In contrast, the heterogeneous pristine sample (c) shows a large amount of pinned dislocation links on the ⊕⊕ group compared to the ⊖⊕ group. Overall, the comparison highlights that both pre-straining and heterogeneous initial dislocation densities among slip systems, modify the prevalence of pinned links on the derived slip system groups.

Appendix I. Effect of cross-slip

In this work, cross-slip is modeled using a thermally activated probabilistic law (Verdier et al., 1998). The probability of cross-slip during a time increment δt is given by

$$P(L) = \frac{\beta L \delta t}{L_0 \delta t_0} \exp\left[\frac{V_{act}}{kT}\left(|\tau| - \tau_{III}\right)\right], \tag{I.1}$$

where β is a normalization constant, V_{act} is the activation volume, and τ_{III} denotes the onset stress for stage-III hardening. The parameters L_0 and δt_0 are reference values for the cross-slipping segment length and time increment, respectively. Here, we employ $\beta = 10^5$, $\tau_{III} = 5\,\text{MPa}$, and $V_{act} = 300b^3$.

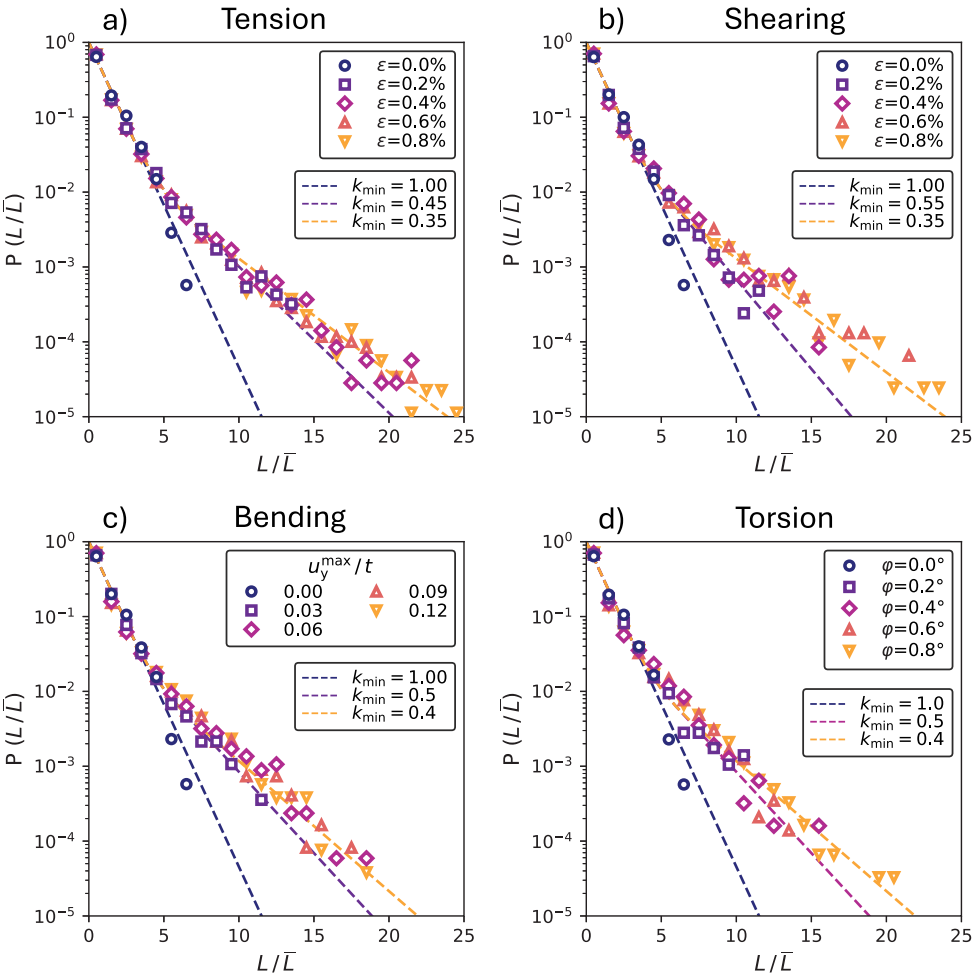

Fig. J.1. The link length distribution evolution in ⟨001⟩ crystal orientation for (a) tension, (b) shearing, (c) bending and (d) torsion at different deformation states.

Fig. I.1 compares the effect of cross-slip for tensile loading in ⟨001⟩ crystal orientation. The mechanical response (a) is resembling with and without cross-slip enabled, whereas the dislocation density multiplication is significantly larger for simulations with cross-slip enabled. The link length distribution (b) is resembling for both scenarios revealing an extended link length distribution aligning to a $k_{\min} = 0.35$.

Appendix J. Evolution of link length distribution

Fig. J.1 illustrates the evolution of the link length distribution starting from an initially relaxed dislocation network for tension, shearing, bending and torsion. The extended link length distribution is already observed at the onset of plastic deformation for each loading condition. With ongoing plasticity, the homogeneous loading scenarios (tension, shearing) reveal an alignment to a $k_{\min}$ of 0.35, whereas the gradient-imposed loading conditions (bending, torsion) align to a $k_{\min}$ of 0.40 at the maximal deformation studied here.

Appendix K. Effect of sample size

Fig. K.1(a) shows that the extended link length distribution is present at different sample sizes. However, for the 1 µm sample, the length distribution lacks statistics due to the existence of only a few dislocation links leading to a scattered probability and a truncation at $L/\bar{L} = 12$. With increasing specimen sizes towards bulk behavior, dislocation links extend further and clearly follow a $k_{\min}$ of ≈ 0.4. In Fig. K.1(b), the size effect of the sample sizes are compared to experimental data of micropillar compression tests from Wu et al. (2016), Kunz et al. (2011), Wang et al. (2012). The DDD simulations show good agreement with the experimentally observed yield stresses with a power law exponent of $m = -0.7$.

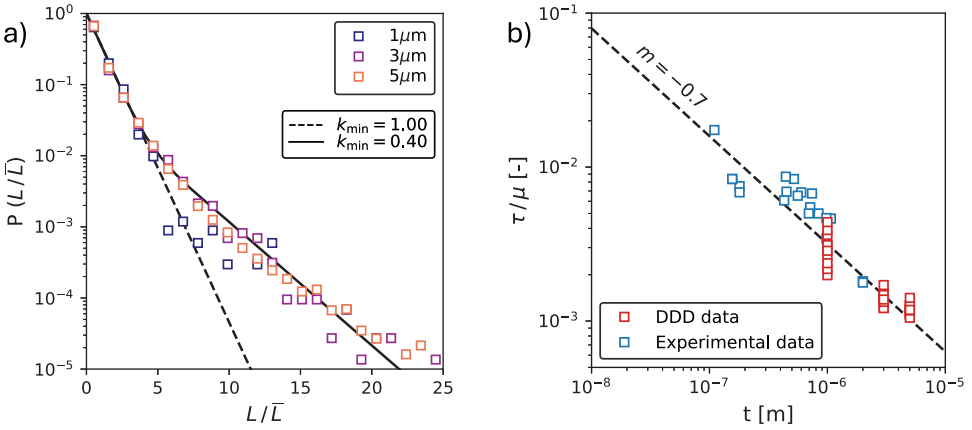

Fig. K.1. (a) The link length distribution in ⟨001⟩ crystal orientation for 1 μm, 3 μm and 5 μm. (b) Size effect of Aluminum micropillars using experimental data from Wu et al. (2016), Kunz et al. (2011), Wang et al. (2012) and DDD simulations revealing a power law with an exponent of $m = -0.7$ for the normalized yield stress τ/μ over thickness t.

Appendix L. Supplementary data

Supplementary material related to this article can be found online at https://doi.org/10.1016/j.ijplas.2026.104744.

Data availability

Data will be made available on request.

References

Akhondzadeh, S., Bertin, N., Sills, R.B., Cai, W., 2021. Slip-free multiplication and complexity of dislocation networks in FCC metals. Mater. Theory 5 (1), http://dx.doi.org/10.1186/s41313-020-00024-y.

Akhondzadeh, S., Zhai, H., Jian, W., Sills, R.B., Bertin, N., Cai, W., 2026. Link statistics of dislocation network during strain hardening. J. Mech. Phys. Solids 106533. http://dx.doi.org/10.1016/j.jmps.2026.106533.

Amelinckx, S., 1956. XXV. The direct observation of dislocation nets in rock salt single crystals. Phil. Mag. 1 (3), 269–290. http://dx.doi.org/10.1080/14786435608238101.

Arsenlis, A., Parks, D., 1999. Crystallographic aspects of geometrically-necessary and statistically-stored dislocation density. Acta Mater. 47 (5), 1597–1611. http://dx.doi.org/10.1016/s1359-6454(99)00020-8.

Bei, H., Shim, S., Pharr, G., George, E., 2008. Effects of pre-strain on the compressive stress–strain response of Mo-alloy single-crystal micropillars. Acta Mater. 56 (17), 4762–4770. http://dx.doi.org/10.1016/j.actamat.2008.05.030.

Berta, D., Katzer, B., Schulz, K., Ispánovity, P.D., 2025a. Predicting plastic deformation of crystalline materials by deciphering acoustic emission. Npj Acoust. 1 (1), http://dx.doi.org/10.1038/s44384-025-00019-4.

Berta, D., Kurunczi-Papp, D., Laurson, L., Ispánovity, P.D., 2025b. On identifying dynamic length scales in crystal plasticity. Acta Mater. 283, 120506. http://dx.doi.org/10.1016/j.actamat.2024.120506.

Bradski, G., 2000. The OpenCV Library. Dr. Dobb's J. Softw. Tools.

Bulatov, V.V., Hsiung, L.L., Tang, M., Arsenlis, A., Bartelt, M.C., Cai, W., Florando, J.N., Hiratani, M., Rhee, M., Hommes, G., Pierce, T.G., de la Rubia, T.D., 2006. Dislocation multi-junctions and strain hardening. Nature 440 (7088), 1174–1178. http://dx.doi.org/10.1038/nature04658.

Carrington, W., Hale, K.F., McLean, D., 1960. Arrangement of dislocations in iron. Proc. R. Soc. Lond. Ser. A. Math. Phys. Sci. 259 (1297), 203–227. http://dx.doi.org/10.1098/rspa.1960.0219.

Castelluccio, G.M., McDowell, D.L., 2017. Mesoscale cyclic crystal plasticity with dislocation substructures. Int. J. Plast. 98, 1–26. http://dx.doi.org/10.1016/j.ijplas.2017.06.002.

Chen, Y.S., Choi, W., Papanikolaou, S., Sethna, J.P., 2010. Bending crystals: Emergence of fractal dislocation structures. Phys. Rev. Lett. 105 (10), 105501. http://dx.doi.org/10.1103/physrevlett.105.105501.

Csikor, F.F., Motz, C., Weygand, D., Zaiser, M., Zapperi, S., 2007. Dislocation avalanches, strain bursts, and the problem of plastic forming at the micrometer scale. Science 318 (5848), 251–254. http://dx.doi.org/10.1126/science.1143719.

Cui, Y., Lin, P., Liu, Z., Zhuang, Z., 2014. Theoretical and numerical investigations of single arm dislocation source controlled plastic flow in FCC micropillars. Int. J. Plast. 55, 279–292. http://dx.doi.org/10.1016/j.ijplas.2013.11.011.

Devincre, B., Hoc, T., Kubin, L., 2008. Dislocation mean free paths and strain hardening of crystals. Science 320 (5884), 1745–1748. http://dx.doi.org/10.1126/science.1156101.

El-Awady, J.A., 2015. Unravelling the physics of size-dependent dislocation-mediated plasticity. Nat. Commun. 6 (1), http://dx.doi.org/10.1038/ncomms6926.

El-Awady, J.A., Uchic, M.D., Shade, P.A., Kim, S.-L., Rao, S.I., Dimiduk, D.M., Woodward, C., 2013. Pre-straining effects on the power-law scaling of size-dependent strengthening in Ni single crystals. Scr. Mater. 68 (3–4), 207–210. http://dx.doi.org/10.1016/j.scriptamat.2012.10.035.

El-Awady, J.A., Wen, M., Ghoniem, N.M., 2009. The role of the weakest-link mechanism in controlling the plasticity of micropillars. J. Mech. Phys. Solids 57 (1), 32–50. http://dx.doi.org/10.1016/j.jmps.2008.10.004.

Franciosi, P., Berveiller, M., Zaoui, A., 1980. Latent hardening in copper and aluminium single crystals. Acta Metall. 28 (3), 273–283. http://dx.doi.org/10.1016/0001-6160(80)90162-5.

Gagel, J., Weygand, D., Gumbsch, P., 2016. Formation of extended prismatic dislocation structures under indentation. Acta Mater. 111, 399–406. http://dx.doi.org/10.1016/j.actamat.2016.04.002.

Gallet, J., Perez, M., Guillou, R., Ernould, C., Le Bourlot, C., Langlois, C., Beausir, B., Bouzy, E., Chaise, T., Cazottes, S., 2023. Experimental measurement of dislocation density in metallic materials: A quantitative comparison between measurements techniques (XRD, R-ECCI, HR-EBSD, TEM). Mater. Charact. 199, 112842. http://dx.doi.org/10.1016/j.matchar.2023.112842.

Gravell, J., Lee, S., Ryu, S., Ryu, I., 2021. Effect of size and orientation on stability of dislocation networks upon torsion loading and unloading in FCC metallic micropillars. Acta Mater. 214 (de-), 117010. http://dx.doi.org/10.1016/j.actamat.2021.117010.

Higashida, K., Takamura, J., Narita, N., 1986. The formation of deformation bands in f.c.c. crystals. Mater. Sci. Eng. 81, 239–258. http://dx.doi.org/10.1016/0025-5416(86)90266-1.

Hirsch, P.B., Horne, R.W., Whelan, M.J., 1956. LXVIII. Direct observations of the arrangement and motion of dislocations in aluminium. Phil. Mag. 1 (7), 677–684. http://dx.doi.org/10.1080/14786435608244003.

Hirsch, P.B., Silcox, J., Smallman, R.E., Westmacott, K.H., 1958. Dislocation loops in quenched aluminium. Phil. Mag. 3 (32), 897–908. http://dx.doi.org/10.1080/14786435808237028.

Hirth, J.P., 1961. On dislocation interactions in the fcc lattice. J. Appl. Phys. 32 (4), 700–706. http://dx.doi.org/10.1063/1.1736074.

Hunter, A., Agrawal, V., Beyerlein, I., Ghosh, S., Oskay, C., Gu, B., Chen, Y., Foster, S.C., Wilkerson, J.W., Sun, X., Rupert, T.J., Chen, C., Dongare, A.M., Blaschke, D.N., Echlin, M.P., Pollock, T.M., Katzer, B., Schulz, K., Croft, Z., Chlupsa, M., Shahani, A.J., Thornton, K., Fullwood, D.T., Homer, E.R., White, E.V., 2026. Roadmap on novel computational approaches for bridging length and time scales: Addressing challenges in modeling processes, characterization, and performance of metals and alloys. Modelling Simul. Mater. Sci. Eng. http://dx.doi.org/10.1088/1361-651x/ae773d.

Hunter, A., Preston, D., 2015. Analytic model of the remobilization of pinned glide dislocations from quasi-static to high strain rates. Int. J. Plast. 70, 1–29. http://dx.doi.org/10.1016/j.ijplas.2015.01.008.

Ispánovity, P.D., Hegyi, Á., Groma, I., Györgyi, G., Ratter, K., Weygand, D., 2013. Average yielding and weakest link statistics in micron-scale plasticity. Acta Mater. 61 (16), 6234–6245. http://dx.doi.org/10.1016/j.actamat.2013.07.007.

Ispánovity, P.D., Laurson, L., Zaiser, M., Groma, I., Zapperi, S., Alava, M.J., 2014. Avalanches in 2D dislocation systems: Plastic yielding is not depinning. Phys. Rev. Lett. 112 (23), 235501. http://dx.doi.org/10.1103/physrevlett.112.235501.

Ispánovity, P.D., Ugi, D., Péterffy, G., Knapek, M., Kalácska, S., Tüzes, D., Dankházi, Z., Máthis, K., Chmelík, F., Groma, I., 2022. Dislocation avalanches are like earthquakes on the micron scale. Nat. Commun. 13 (1), http://dx.doi.org/10.1038/s41467-022-29044-7.

Jeong, J., Voyiadjis, G.Z., 2022. A physics-based crystal plasticity model for the prediction of the dislocation densities in micropillar compression. J. Mech. Phys. Solids 167, 105006. http://dx.doi.org/10.1016/j.jmps.2022.105006.

Katzer, B., Betsche, D., Böhm, K., Weygand, D., Schulz, K., 2024a. A graph database for feature characterization of dislocation networks. Scr. Mater. 240, 115841. http://dx.doi.org/10.1016/j.scriptamat.2023.115841.

Katzer, B., Betsche, D., von Hoegen, F., Jochum, B., Böhm, K., Schulz, K., 2024b. Combining simulation and experimental data via surrogate modelling of continuum dislocation dynamics simulations. Modelling Simul. Mater. Sci. Eng. 32 (5), 055026. http://dx.doi.org/10.1088/1361-651x/ad4b4c.

Katzer, B., Zoller, K., Bermuth, J., Weygand, D., Schulz, K., 2023. Characterization of Lomer junctions based on the Lomer arm length distribution in dislocation networks. Scr. Mater. 226, 115232. http://dx.doi.org/10.1016/j.scriptamat.2022.115232.

Katzer, B., Zoller, K., Weygand, D., Schulz, K., 2022. Identification of dislocation reaction kinetics in complex dislocation networks for continuum modelling using data-driven methods. J. Mech. Phys. Solids 168, 105042. http://dx.doi.org/10.1016/j.jmps.2022.105042.

Kohnert, A.A., Capolungo, L., 2022. The kinetics of static recovery by dislocation climb. Npj Comput. Mater. 8 (1), http://dx.doi.org/10.1038/s41524-022-00790-y.

Kunz, A., Pathak, S., Greer, J.R., 2011. Size effects in Al nanopillars: Single crystalline vs. bicrystalline. Acta Mater. 59 (11), 4416–4424. http://dx.doi.org/10.1016/j.actamat.2011.03.065.

Lamari, M., Kerfriden, P., Salman, O., Yastrebov, V., Ammar, K., Forest, S., 2025. A time-discontinuous elasto-plasticity formalism to simulate instantaneous plastic flow bursts. Int. J. Solids Struct. 309, 113171. http://dx.doi.org/10.1016/j.ijsolstr.2024.113171.

Lee, S.-W., Han, S.M., Nix, W.D., 2009. Uniaxial compression of fcc Au nanopillars on an MgO substrate: The effects of prestraining and annealing. Acta Mater. 57 (15), 4404–4415. http://dx.doi.org/10.1016/j.actamat.2009.06.002.

Li, Y., Ding, Y., Li, C.-e., Ren, J., Ran, G., 2023. Dislocations generated by pre-strain dominate the subsequent plastic deformation. Mater. Sci. Eng.: A 887, 145716. http://dx.doi.org/10.1016/j.msea.2023.145716.

Madec, R., Devincre, B., Kubin, L., Hoc, T., Rodney, D., 2003. The role of collinear interaction in dislocation-induced hardening. Science 301 (5641), 1879–1882. http://dx.doi.org/10.1126/science.1085477.

McDowell, D.L., 2025. Nonequilibrium thermodynamics, kinetics, and self-organization of dislocation avalanche plasticity. Int. J. Plast. 195, 104504. http://dx.doi.org/10.1016/j.ijplas.2025.104504.

McElfresh, C., Cui, Y., Dudarev, S.L., Po, G., Marian, J., 2021. Discrete stochastic model of point defect-dislocation interaction for simulating dislocation climb. Int. J. Plast. 136, 102848. http://dx.doi.org/10.1016/j.ijplas.2020.102848.

Motz, C., Weygand, D., Senger, J., Gumbsch, P., 2008. Micro-bending tests: A comparison between three-dimensional discrete dislocation dynamics simulations and experiments. Acta Mater. 56 (9), 1942–1955. http://dx.doi.org/10.1016/j.actamat.2007.12.053.

Motz, C., Weygand, D., Senger, J., Gumbsch, P., 2009. Initial dislocation structures in 3-D discrete dislocation dynamics and their influence on microscale plasticity. Acta Mater. 57 (6), 1744–1754. http://dx.doi.org/10.1016/j.actamat.2008.12.020.

Papanikolaou, S., Cui, Y., Ghoniem, N., 2017. Avalanches and plastic flow in crystal plasticity: an overview. Modelling Simul. Mater. Sci. Eng. 26 (1), 013001. http://dx.doi.org/10.1088/1361-651x/aa97ad.

Roters, F., Diehl, M., Shanthraj, P., Eisenlohr, P., Reuber, C., Wong, S., Maiti, T., Ebrahimi, A., Hochrainer, T., Fabritius, H.-O., Nikolov, S., Friák, M., Fujita, N., Grilli, N., Janssens, K., Jia, N., Kok, P., Ma, D., Meier, F., Werner, E., Stricker, M., Weygand, D., Raabe, D., 2019. DAMASK – The Düsseldorf Advanced Material Simulation Kit for modeling multi-physics crystal plasticity, thermal, and damage phenomena from the single crystal up to the component scale. Comput. Mater. Sci. 158, 420–478. http://dx.doi.org/10.1016/j.commatsci.2018.04.030.

Ruestes, C.J., Segurado, J., 2024. A stochastic discrete slip approach to microplasticity: Application to submicron W pillars. Int. J. Plast. 176, 103965. http://dx.doi.org/10.1016/j.ijplas.2024.103965.

Schneider, A., Kiener, D., Yakacki, C., Maier, H., Gruber, P., Tamura, N., Kunz, M., Minor, A., Frick, C., 2013. Influence of bulk pre-straining on the size effect in nickel compression pillars. Mater. Sci. Eng.: A 559, 147–158. http://dx.doi.org/10.1016/j.msea.2012.08.055.

Schulz, K., Wagner, L., Wieners, C., 2019. A mesoscale continuum approach of dislocation dynamics and the approximation by a Runge-Kutta discontinuous Galerkin method. Int. J. Plast. 120, 248–261. http://dx.doi.org/10.1016/j.ijplas.2019.05.003.

Senger, J., Weygand, D., Kraft, O., Gumbsch, P., 2011a. Dislocation microstructure evolution in cyclically twisted microsamples: a discrete dislocation dynamics simulation. Modelling Simul. Mater. Sci. Eng. 19 (7), 074004. http://dx.doi.org/10.1088/0965-0393/19/7/074004.

Senger, J., Weygand, D., Motz, C., Gumbsch, P., Kraft, O., 2011b. Aspect ratio and stochastic effects in the plasticity of uniformly loaded micrometer sized specimens. Acta Mater. 59 (8), 2937–2947. http://dx.doi.org/10.1016/j.actamat.2011.01.034, 43.12.03; LK 01.

Shishvan, S.S., der Giessen, E.V., 2010. Distribution of dislocation source length and the size dependent yield strength in freestanding thin films. J. Mech. Phys. Solids 58 (5), 678–695. http://dx.doi.org/10.1016/j.jmps.2010.02.011.

Sills, R.B., Bertin, N., Aghaei, A., Cai, W., 2018. Dislocation networks and the microstructural origin of strain hardening. Phys. Rev. Lett. 121 (8), 085501. http://dx.doi.org/10.1103/physrevlett.121.085501.

Sills, R.B., Foster, M.E., Zhou, X.W., 2020. Line-length-dependent dislocation mobilities in an FCC stainless steel alloy. Int. J. Plast. 135, 102791. http://dx.doi.org/10.1016/j.ijplas.2020.102791.

Song, H., Yavas, H., der Giessen, E.V., Papanikolaou, S., 2019. Discrete dislocation dynamics simulations of nanoindentation with pre-stress: Hardness and statistics of abrupt plastic events. J. Mech. Phys. Solids 123, 332–347. http://dx.doi.org/10.1016/j.jmps.2018.09.005.

Stricker, M., Weygand, D., 2015. Dislocation multiplication mechanisms – Glissile junctions and their role on the plastic deformation at the microscale. Acta Mater. 99, 130–139. http://dx.doi.org/10.1016/j.actamat.2015.07.073.

Stricker, M., Ziemann, M., Walter, M., Weygand, S.M., Gruber, P., Weygand, D., 2022. Dislocation structure analysis in the strain gradient of torsion loading: a comparison between modelling and experiment. Modelling Simul. Mater. Sci. Eng. 30 (3), http://dx.doi.org/10.1088/1361-651X/ac4d77, Art.Nr.: 035007. 43.31.01; LK 01.

Sudmanns, M., Bach, J., Weygand, D., Schulz, K., 2020. Data-driven exploration and continuum modeling of dislocation networks. Modelling Simul. Mater. Sci. Eng. 28 (6), 065001. http://dx.doi.org/10.1088/1361-651x/ab97ef.

Sudmanns, M., Stricker, M., Weygand, D., Hochrainer, T., Schulz, K., 2019. Dislocation multiplication by cross-slip and glissile reaction in a dislocation based continuum formulation of crystal plasticity. J. Mech. Phys. Solids 132, 103695. http://dx.doi.org/10.1016/j.jmps.2019.103695.

Tan, J., Villa, U., Shamsaei, N., Shao, S., Zbib, H.M., Faghihi, D., 2021. A predictive discrete-continuum multiscale model of plasticity with quantified uncertainty. Int. J. Plast. 138, 102935. http://dx.doi.org/10.1016/j.ijplas.2021.102935.

Taylor, G., 1934. The mechanism of plastic deformation of crystals. Part I.—Theoretical. Proc. R. Soc. Lond. Ser. A Contain. Pap. A Math. Phys. Character 145 (855), 362–387. http://dx.doi.org/10.1098/rspa.1934.0106.

Verdier, M., Fivel, M., Groma, I., 1998. Mesoscopic scale simulation of dislocation dynamics in fcc metals: Principles and applications. Modelling Simul. Mater. Sci. Eng. 6 (6), 755–770. http://dx.doi.org/10.1088/0965-0393/6/6/007.

Vivekanandan, V., Lin, P., Winther, G., El-Azab, A., 2021. On the implementation of dislocation reactions in continuum dislocation dynamics modeling of mesoscale plasticity. J. Mech. Phys. Solids 149, 104327. http://dx.doi.org/10.1016/j.jmps.2021.104327.

Voyiadjis, G.Z., Yaghoobi, M., 2017. Size and strain rate effects in metallic samples of confined volumes: Dislocation length distribution. Scr. Mater. 130, 182–186. http://dx.doi.org/10.1016/j.scriptamat.2016.12.001.

Wang, F., Guo, J., Weygand, D., Wang, F., Rupert, T.J., Chen, D., Gianola, D.S., 2024. Topology and evolution of dislocation structures mediated by glissile reactions in face-centered cubic metals. Acta Mater. 268, 119748. http://dx.doi.org/10.1016/j.actamat.2024.119748.

Wang, Z.-J., Li, Q.-J., Shan, Z.-W., Li, J., Sun, J., Ma, E., 2012. Sample size effects on the large strain bursts in submicron aluminum pillars. Appl. Phys. Lett. 100 (7), http://dx.doi.org/10.1063/1.3681582.

Weinberger, C.R., Cai, W., 2010. Plasticity of metal wires in torsion: Molecular dynamics and dislocation dynamics simulations. J. Mech. Phys. Solids 58 (7), 1011–1025. http://dx.doi.org/10.1016/j.jmps.2010.04.010.

Weinberger, C.R., Cai, W., 2011. The stability of Lomer–Cottrell jogs in nanopillars. Scr. Mater. 64 (6), 529–532. http://dx.doi.org/10.1016/j.scriptamat.2010.11.037.

Weygand, D., Friedman, L., van der Giessen, E., Needleman, A., 2001. Discrete dislocation modeling in three-dimensional confined volumes. Mater. Sci. Eng.: A 309–310, 420–424. http://dx.doi.org/10.1016/s0921-5093(00)01632-4.

Weygand, D., Friedman, L.H., der Giessen, E.V., Needleman, A., 2002. Aspects of boundary-value problem solutions with three-dimensional dislocation dynamics. Modelling Simul. Mater. Sci. Eng. 10 (4), 437–468. http://dx.doi.org/10.1088/0965-0393/10/4/306.

Weygand, D., Gumbsch, P., 2005. Study of dislocation reactions and rearrangements under different loading conditions. Mater. Sci. Eng.: A 400–401, 158–161. http://dx.doi.org/10.1016/j.msea.2005.03.102.

Weygand, D., Senger, J., Motz, C., Augustin, W., Heuveline, V., Gumbsch, P., 2008. High Performance computing and discrete dislocation dynamics: Plasticity of micrometer sized specimens. In: Nagel, W. (Ed.), High Performance Computing in Science and Engineering '08. Springer-Verlag, pp. 507–523. http://dx.doi.org/10.1007/978-3-540-88303-6_36.

Wijnen, J., Hoefnagels, J., Geers, M., Peerlings, R., 2025. Discrete slip plane analysis of ferrite microtensile tests: Influence of dislocation source distribution and non-schmid effects on slip system activity. Mater. Des. 251, 113698. http://dx.doi.org/10.1016/j.matdes.2025.113698.

Wijnen, J., Peerlings, R., Hoefnagels, J., Geers, M., 2021. A discrete slip plane model for simulating heterogeneous plastic deformation in single crystals. Int. J. Solids Struct. 228, 111094. http://dx.doi.org/10.1016/j.ijsolstr.2021.111094.

Wu, J., Tsai, W., Huang, J., Hsieh, C., Huang, G.-R., 2016. Sample size and orientation effects of single crystal aluminum. Mater. Sci. Eng.: A 662, 296–302. http://dx.doi.org/10.1016/j.msea.2016.03.076.

Ye, C., Liu, G., Chen, K., Liu, J., Hu, J., Yu, Y., Mao, Y., Shen, Y., 2023a. Strain-rate dependent crystal plasticity model and aluminum softening/hardening transition. Comput. Mater. Sci. 222, 112108. http://dx.doi.org/10.1016/j.commatsci.2023.112108.

Ye, C., Liu, G., Chen, K., Liu, J., Hu, J., Yu, Y., Mao, Y., Shen, Y., 2023b. Unified crystal plasticity model for fcc metals: From quasistatic to shock loading. Phys. Rev. B 107 (2), 024105. http://dx.doi.org/10.1103/physrevb.107.024105.

Zepeda-Ruiz, L.A., Stukowski, A., Oppelstrup, T., Bertin, N., Barton, N.R., Freitas, R., Bulatov, V.V., 2020. Atomistic insights into metal hardening. Nat. Mater. 20 (3), 315–320. http://dx.doi.org/10.1038/s41563-020-00815-1.

Zhang, Y., Sills, R.B., 2024. Junction formation rates, residence times, and the rate of plastic flow in FCC metals. J. Mater. Sci.: Mater. Theory 8 (1), http://dx.doi.org/10.1186/s41313-024-00063-9.